Geomorphic response to the Lateglacial-Holocene transition in high Alpine regions (Sanetsch Pass, Swiss Alps)

Elena Serra, Pierre G Valla, Natacha Gribenski, Fabio J Guedes Magrani, Julien Carcaillet, Reynald Delaloye, Bernard Grobéty, Luc Braillard

Accepted Manuscript published at Boreas
(doi.org/10.1111/bor.12480)

Geomorphic response to the Lateglacial-Holocene transition in high Alpine regions (Sanetsch Pass, Swiss Alps)

ELENA SERRA, PIERRE G. VALLA, NATACHA GRIBENSKI, FABIO J. GUEDES MAGRANI, JULIEN CARCAILLET, REYNALD DELALOYE, BERNARD GROBÉTY AND LUC BRAILLARD

Serra, E., Valla, P. G., Gribenski, N., Guedes Magrani, F. J., Carcaillet, J., Delaloye, R., Grobéty, B. & Braillard, L.: Geomorphic response to the Lateglacial-Holocene transition in high Alpine regions (Sanetsch Pass, Swiss Alps)

Several palaeoclimatic archives have documented the pronounced climatic and environmental change associated with the Lateglacial-Holocene transition in the European Alps. However, the geomorphic response to this major environmental transition has been only punctually investigated. In this study, we propose a detailed reconstruction of post-Last Glacial Maximum palaeo-environmental conditions and geomorphic connectivity in the Sanetsch Pass area (2252 m a.s.l., western Swiss Alps), based on a multi-method approach combining geomorphological and sedimentological field investigations with quantitative sedimentology and geochronology. Samples for sediment characterization (grain-size, micromorphology and X-Ray diffraction) and geochronology (optically stimulated luminescence and ^{10}Be surface exposure dating) were collected from three representative landforms of the study area: a high-elevation silty deposit covered by patterned ground, an alluvial fan and a hummocky moraine covered by rockfall deposits. Our multi-method outcomes reveal the geomorphic history of the three deposits and

Accepted Manuscript published at Boreas
(doi.org/10.1111/bor.12480)

their connectivity through sediment cascade. These results highlight the development of rapid and most probably transient landscape changes in high Alpine regions during the Lateglacial-Holocene transition, with an increase in sediment flux and the establishment of paraglacial and periglacial geomorphic processes.

Elena Serra *(elena.serra@geo.unibe.ch), **Natacha Gribenski and Fabio J. Guedes Magrani**, Institute of Geological Sciences, University of Bern, Baltzerstrasse 1+3, CH-3012 Bern, Switzerland, and Oeschger Centre for Climate Change Research, University of Bern, Hochschulstrasse 4, CH-3012 Bern, Switzerland; **Pierre G. Valla**, University of Grenoble Alpes, University of Savoie Mont Blanc, CNRS, IRD, IFSTTAR, ISTerre, 38000 Grenoble, France, and Institute of Geological Sciences, University of Bern, Baltzerstrasse 1+3, CH-3012 Bern, Switzerland, and Oeschger Centre for Climate Change Research, University of Bern, Hochschulstrasse 4, CH-3012 Bern, Switzerland; **Julien Carcaillet**, University of Grenoble Alpes, University of Savoie Mont Blanc, CNRS, IRD, IFSTTAR, ISTerre, 38000 Grenoble, France; **Reynald Delaloye**, **Bernard Grobéty and Luc Braillard,** Department of Geosciences, University of Fribourg, Ch. du Musée 4+6, CH-41700 Fribourg, Switzerland.*

Accepted Manuscript published at Boreas
(doi.org/10.1111/bor.12480)

High-elevation Alpine regions are active environments, where landforms are constantly re-shaped by the interplay between a variety of geomorphic processes. Throughout the Quaternary, the nature and dominance of these processes have been largely determined by climatic oscillations between glacial and interglacial conditions. During glacial periods, glacier erosion, sediment transport and deposition leave behind characteristic landforms and deposits such as U-shaped valleys, glacial cirques, polished bedrock, moraines and erratic boulders (e.g. Benn & Evans 2014). During or soon after glacier retreat at the glacial/interglacial transition, glacial processes are gradually replaced by paraglacial and periglacial processes, which transiently transform the ice-free landscape (Church & Ryder 1972; Ballantyne 2002; French 2007; Mercier & Etienne 2008). Paraglacial processes involve various geomorphic agents (hillslope, fluvial, aeolian) resulting in a wide range of depositional and erosional landforms (e.g. rockfall deposits, debris cones, alluvial fans, gully incisions and aeolian drapes; Ballantyne 2002; Cossart *et al.* 2008; Borgatti & Soldati 2010; Cossart *et al.* 2013; Geilhausen *et al.* 2013; Gild *et al.* 2018). Periglacial processes are also present and give origin to permafrost-related landforms like rock glaciers and patterned ground (French 2007; Colombo *et al.* 2016).

The European Alps have been repeatedly glaciated during the Late Pleistocene, with glacier expansion culminating at the Last Glacial Maximum (LGM, 26.5-19.0 ka ago; Clark *et al.* 2009; Wirsig *et al.* 2016a). Post-LGM warming and rapid ice decay were followed by episodes of glacier stillstands and readvances during the Lateglacial period (Lateglacial stadials, 19.0-11.6 ka ago; Ivy-Ochs *et al*. 2007; Hippe *et al.* 2014; Ivy-Ochs 2015), due to temporary climate deteriorations (Schmidt *et al.* 2012). Following the Younger Dryas (YD, 12.7-11.6 ka ago; Ivy-Ochs *et al.* 2007) and the Early Holocene Preboreal Oscillation cold event (11.4-11.3 ka ago; Rasmussen *et al.* 2007; Schimmelpfennig *et al.* 2012), Alpine glaciers eventually retreated

Accepted Manuscript published at Boreas
(doi.org/10.1111/bor.12480)

and remained behind ice limit of the Little Ice Age (LIA, 1300-1860 CE; Hanspeter *et al.* 2005; Ivy-Ochs *et al.* 2009; Steinemann *et al.* 2020), in response to Early and Middle Holocene abrupt warming (Schimmelpfennig *et al.* 2012).

Palaeoenvironmental conditions during the Lateglacial and at the Holocene transition have been investigated through several palaeoclimate proxies (Heiri *et al.* 2014). However, the geomorphic response to this major environmental transition has been only punctually examined, focusing on specific geomorphic processes like rockfall activity (e.g. Zerathe *et al.* 2014; Ivy-Ochs *et al.* 2017) or fluvial incision (e.g. Korup & Schlunegger 2007; Valla *et al.* 2010; Rolland *et al.* 2017). Likewise, the timing of paraglacial activity, as well as the question of sediment cascade and landscape connectivity, are still poorly understood (Mercier & Etienne 2008 and references therein).

Our study aimed to contribute to the reconstruction of post-LGM palaeoenvironmental conditions and geomorphic connectivity within high-altitude Alpine regions. We focused on the Sanetsch Pass area (2252 m a.s.l., western Swiss Alps; Fig. 1) where multiple geomorphic processes have left an extensive record of landforms and sediment deposits during the Lateglacial and the Holocene (Fig. 2). Three landforms representative of the high Alpine landscape were investigated: a silty deposit covered by patterned ground, an alluvial fan and a hummocky moraine covered by rockfall deposits (Figs 1, 2, 3). These three deposits were selected with the goals of (i) reconstructing their geomorphological history, (ii) investigating a potential connectivity between the different records and (iii) assessing the suitability of glacial, paraglacial and periglacial landforms as proxies for palaeoenvironmental reconstruction in high Alpine regions. To that aim, we performed a detailed geomorphological and sedimentological

field investigation and collected samples for multi-methodological analyses on the different landforms.

Study area and sampling locations

The study area is located next to the Sanetsch Pass (2252 m a.s.l., western Swiss Alps; Fig. 1). The local bedrock is composed of Cretaceous and Paleogene sedimentary rocks belonging to the Helvetic Diablerets and Wildhorn nappes (Badoux *et al.* 1959; Masson *et al.* 1980). Three geological units are of particular interest for our study: calcareous shales containing ca. 20% of fine detrital quartz (Palfris Formation; Föllmi *et al.* 2007) form the Arpille Ridge, siliceous limestones (Helvetic Kieselkalk Formation; Föllmi *et al.* 2007) form the Arpelistock cliff, and quartzose sandstones (Fruttli Member of the Klimsenhorn Formation, Menkveld-Gfeller 1997) from a 5-m thick layer at the top of the calcareous Les Montons cliff (Fig. 2).

The Sanetsch Pass is currently ice free, with the nearest glacier front (Tsanfleuron Glacier) 3 km to the southwest (Fig. 1). During the LGM, the Rhône glacier reached an altitude of about 2000 m a.s.l. in the main valley above Sion (Fig. 1; Bini *et al.* 2009). The Sanetsch Pass area was partly covered by ice with an estimated average thickness of 200 m and some mountain peaks were protruding above the ice surface as nunataks (Bini *et al.* 2009). The Tsanfleuron glacier was flowing both northwards and southwards from the pass, as testified by lateral morainic ridges (Fig. 2; Badoux *et al.* 1959). Following the deglaciation of the Swiss foreland *c.* 21 ka ago (Ivy-Ochs *et al.* 2004), the Rhône Valley became ice free *c.* 17 ka ago (Hantke 1992; Hinderer 2001). The onset of sedimentation in the Pond Emines (at 2288 m a.s.l., 1 km southwest from the Sanetsch Pass; Fig. 2) at *c.* 12 ka ago (Berthel *et al.* 2012), and the apparent post-12 ka exposure ages (Steinemann *et al.* 2020) of glacially-polished bedrock outside

the Tsanfleuron LIA moraine (1 km west of the Sanetsch Pass; Fig. 2) imply ice-free conditions at the Sanetsch Pass during or soon after the YD. Paraglacial and periglacial processes following the deglaciation have resulted in a rich record of landforms reflecting the transient landscape evolution (Fig. 2). Three representative landforms of the Sanetsch Pass landscape are investigated in the present study (Figs 2, 3).

The first landform consists of a thin sediment blanket draping a bedrock platform located on the southern slope of the Arpelistock peak, in contact with glacial deposit from a small local glacier (ARP site, 2660-2715 m a.s.l., 0.23 km^2 in area; Fig. 3A). The surface of the ARP deposit exhibits locally a polygonal patterned ground (Fig. 3B; Gobat & Guenat 2019). The second landform is an alluvial fan located in the plain north of the Sanetsch Pass (CRE site, 2090-2130 m a.s.l., 0.14 km^2 in area; Fig. 3A, C). The third landform is a hummocky moraine located north of the plain (SAN site, 2040-2100 m a.s.l., 0.13 km^2 in area; Figs. 3A, C, D). The distinct hummocky morphology, with hills up to a few meters high, is partially covered by rockfall deposits composed of sandstone and limestone boulders detached from the nearby overhanging cliff (Les Montons peak; Figs 2, 3D).

Methods

Geomorphological and sedimentological field investigation

In the present study, we performed a new geomorphological mapping over an area of 16 km^2 around the Sanetsch pass (Fig. 2), based on the sheet St-Léonard (1286) (Badoux *et al.* 1959) of the Geological Atlas of Switzerland (1:25000). To this aim, we combined the geomorphological map of Quaternary superficial deposits (Badoux *et al.* 1959) with new field investigations and remote sensing mapping based on the swissALTI3D DEM and orthophotos (swisstopo).

Detailed stratigraphic outcrops were logged for the ARP and CRE deposits. Two stratigraphic profiles (40 cm-deep) were dug out in the ARP high-elevation silty deposit, below the polygonal patterned ground (Fig. 3B). The CRE log was recorded from a natural outcrop exposed in a gully incising the alluvial fan (4.5 m deep; Fig. 3C). Sedimentary units were identified based on their grain-size range, sorting, clast shape, compaction, sedimentary structures, colour and lithology. Reaction to HCl on the field and nature of contacts between individual units were also recorded.

Grain-size, micromorphology and optical petrography

Eight bulk sediment samples were collected for grain-size analyses (G1-G6 from CRE site, G7 and G8 from ARP site; Figs 5 and 4, respectively), in order to understand the genesis of the ARP and CRE deposits and a potential connectivity between them. Conventional grain-size distribution measurements were carried out by sieving the air-dried sand and granule/pebble fractions (Rivière 1977; Hadjouis 1987). Analyses of the silt and clay fractions were performed using a laser Malvern MS20 diffraction system (Department of Environmental Sciences, University of Basel, Switzerland). Sorting indexes (So) were calculated using millimetres units ($So = (D_{75}/D_{25})^{0.5}$, where D_{25} and D_{75} are respectively the first and the third quartile of the grain-size distribution), providing different sediment sorting categories: very well sorted ($So < 2.5$), well sorted (So between 2.5 and 3.5), normally sorted (So between 3.5 and 4.5) and poorly sorted ($So > 4.5$).

Three CRE undisturbed sediment samples were collected in Kubiena boxes (8x11 cm) for micromorphological analyses (M1-M3; Fig. 5), with the aim to identify depositional and post-depositional features in the alluvial fan sediments. The samples were first air-dried, impregnated

154 with an acetone-diluted epoxy resin and then cut with a diamond saw (Department of
155 Environmental Sciences, University of Basel, Switzerland). Two covered thin sections (4.5x4.5
156 cm) per sample were prepared (Th. Beckmann, Braunschweig, Germany) and examined optically
157 on a Leitz DM-RXP microscope, both in plane-polarized and crossed-polarized light. Bedrock
158 thin sections were additionally prepared (Department of Geosciences, University of Fribourg,
159 Switzerland) and analysed for four bedrock samples representative of the catchment lithology
160 (two from the siliceous limestone, L1 and L2, and two from the calcareous shale, S1 and S2;
161 Table S1), in order to obtain further information on the silicate fraction of the bedrock (grain
162 shape and size) and to discuss a potential connectivity between the local bedrock and the CRE
163 sediments.
164
165 X-Ray diffraction and geochemistry
166 X-Ray Diffraction (XRD) analyses were performed on a total of 22 samples, including 18 bulk
167 sediment samples from CRE and ARP sites (CRE01-CRE16, Fig. 5; ARP01 and ARP03, Fig. 4)
168 and 4 bedrock samples (L1, L2, S1, S2), to gain information on their mineral composition and
169 assess sediment provenance and potential connectivity of the ARP and CRE deposits. Bulk
170 sediments and bedrock samples were ground with a mechanical crusher, and sample powders
171 were analysed through a Rigaku Ultima IV diffractometer system using Cu-Kα radiation
172 (Department of Geosciences, University of Fribourg, Switzerland). Mineral identification was
173 performed using the Rigaku's PDXL-2 software and the ICDD Powder Diffraction File 2017
174 database (International Centre for Diffraction Data). Mineral quantification was made by
175 Rietveld refinement (Rietveld 1969), with weighted residuals of the whole pattern (Rwp) and the

goodness of fit (GOF) considered as Rietveld fit criteria (Toby 2006). In the present refinements, Rwp and GOF values range from 4.84% to 6.74% and from 1.73 to 2.90, respectively.

Concentrations of total carbon (TC) and total inorganic carbon (TIC) were measured on the same ARP and CRE sediment samples, using a Bruker G4 Icarus elemental analyser (Institute of Geology, University of Bern, Switzerland). The percentage of total organic carbon (TOC) was determined from the difference between TC and TIC. These analyses and calculations were performed to examine the potential presence of palaeosols in the deposits.

Geochronology

Portable optically stimulated luminescence. Luminescence signal intensities were measured for the CRE (cre01-cre16; Fig. 5) and ARP (arp01-arp05; Fig. 4) sites, with the aim of investigating potential stratigraphic variation in the luminescence response, possibly reflecting differences in sediment provenance and depositional environment. Indeed, the luminescence signal of bulk sediment is mainly dependent, among other factors, on the pre-deposition light exposure of sediments (i.e. signal resetting or " bleaching"; King *et al.* 2014) and on the post-deposition signal accumulation during burial time due to surrounding irradiation (i.e. sediment age; Sanderson & Murphy 2010). Few grams of sample were collected at different depths along the ARP and CRE stratigraphy, and sealed from light exposure. We quantified total photon counts on two replicates of each bulk sediment sample (without chemical pre-treatment) using the SUERC portable OSL reader (Sanderson & Murphy 2010), following the measurement sequence of Muñoz-Salinas *et al.* (2014). The measurement sequence (150 s in total) comprises a first cycle of infrared-stimulated luminescence, targeting feldspar minerals within the bulk sediment (IRSL, 30 s), and a second cycle of blue-stimulated luminescence targeting quartz (hereafter

referred to as optically-stimulated luminescence, OSL, 60 s), separated by 10 s of dark counts. Two additional periods (10 s) of dark counts bracketed each measurement sequence. Final (IRSL and OSL) photon counts were obtained by averaging between the two replicate measurements of each sediment sample.

Conventional optically stimulated luminescence dating. Seven fine-grain samples were collected for conventional luminescence dating from the CRE alluvial fan (CRE01-CRE04; Fig. 5) and the ARP high-elevation platform (ARP01-ARP03; Fig. 4), to constrain sediment deposition chronology. By combining conventional and portable luminescence measurements, we determined the true depositional chronology of the deposits, taking into account potential pre-depositional partial bleaching or post-depositional sediment reworking (i.e. resulting in age overestimation or underestimation, respectively).

Samples were collected with opaque plastic tubes pounded into fresh sediment surface (Nelson *et al.* 2015). Under subdued laboratory illumination, samples were treated with HCl (32%) and H_2O_2 (30%) to remove carbonates and organic components, respectively. Sedimentation in Atterberg cylinders (based on Stokes' Law) was used to extract the 4-11 μm grain-size fraction. Half of the extracted 4-11 μm fraction was additionally treated with H_2SiF_6 (30%) to obtain pure quartz (only ARP03 did not provide enough material for quartz purification). Polymineral and quartz separates were settled on 10-mm diameter stainless steel discs for subsequent luminescence analyses.

All conventional luminescence measurements were carried out using TL/OSL DA-20 Risø readers, equipped with a calibrated $^{90}Sr/^{90}Y$ beta source (Institute of Geology, University of Bern, Switzerland). Luminescence signals were detected using an EMI 9235QA photomultiplier

tube, in the UV region through a 7.5 mm of Hoya U-340 transmission filter and in the blue region through a Schott BG-39 and L.O.T.-Oriel D410/30nm filter combination, for quartz OSL and polymineral IRSL measurements respectively.

OSL and/or IRSL measurements were performed according to sample mineral composition. OSL equivalent dose (D_e) measurements were conducted on quartz separates of two ARP samples (ARP01 and ARP02) and on all the CRE samples. A post-IR OSL protocol was applied (Table S2A), which includes an IRSL stimulation at 50 °C (100 s) prior to the blue OSL stimulation (at 125 °C for 100 s; Lowick *et al.* 2015). IRSL D_e measurements were conducted on polymineral (non-separated) fractions for all the ARP samples using the post-IR IRSL protocol of Buylaert *et al.* (2009) (this protocol targets feldspar luminescence signal only; Table S2B). After a preheat treatment (250 °C for 60 s), luminescence measurement cycles of this modified single-aliquot regenerative (SAR) dose protocol (Murray & Wintle 2000) consist in a first IRSL stimulation at 50 °C (100 s) followed by a second IRSL stimulation at 225 °C (100 s). A 40s IRSL stimulation at 290 °C was added at the end of each SAR cycle in order to limit signal carry-over throughout successive cycles (Wallinga *et al.* 2007). No post-IR IRSL measurements were performed on CRE samples due to the absence of feldspar IRSL signal. Fading rates (*g-value*; Aitken 1985) were measured on aliquots used for D_e determination, following Auclair *et al.* (2003). Final fading corrected D_e values were calculated following the fading correction procedure of Huntley & Lamothe (2011), using the Luminescence R package (Kreutzer *et al.* 2012). Signals used for data analysis were integrated over the first 1.2-2.4 s minus the following 2.6-8 s for quartz OSL measurements, and over the first 1.2-10 s minus the last 90-99 s for polymineral IRSL measurements. Dose–response curves were constructed using an exponential fitting. Recycling ratios within 15% of unity and recuperation within 10% of the

natural dose were used as acceptance criteria for the single-aliquot data. The suitability of the two applied protocols was confirmed by preheat-plateau (for quartz OSL), and residual and dose-recovery tests (Wintle & Murray 2006). For all the samples, residual doses <2% of the natural D_e and recovered doses within 10% of the unity were measured.

About 200 g of bulk sediment material were collected from the surrounding of each sample to determine the environmental dose rate. The material was desiccated at 60 °C to enable water content quantification. U, Th and K activities were measured using high-resolution gamma spectrometry (Department of Chemistry and Biochemistry, University of Bern, Switzerland; Preusser & Kasper 2001) and were employed, together with the water content, as inputs for final dose rate determination through the Dose Rate and Age Calculator (DRAC; Durcan *et al.* 2015). Final ages were calculated using the Central Age Model (CAM; Galbraith & Roberts 2012).

^{10}Be surface exposure dating. Three sandstone boulders rockfall-derived lying on the hummocky moraine, one on a flat area, one on a hummock ridge and one in an intra-hummock hollow (boulders □ 2-m wide and 1-m high, SAN site; Fig. 3C), were sampled for ^{10}Be surface-exposure dating, in order to obtain a minimum age constraint for the hummocky moraine formation. Samples were collected with hammer and chisel from flat surfaces on top of the boulders, with evidence for minimal erosion (Gosse & Phillips 2001). Sample crushing and sieving were performed to isolate the 250-400 μm grainsize fraction. Quartz was isolated using magnetic separation and repeated leaching in a H_2SiF_6-HCl mixture. Conventional chemical treatment adapted from Brown *et al.* (1991) and Merchel & Herpers (1999) was followed to complete ^{10}Be extraction (GTC platform, ISTerre, University Grenoble Alpes, France). ^{10}Be/^{9}Be ratios were measured at ASTER French National AMS facility (CEREGE, Aix-en-Provence, France; Arnold

et al. 2010) against the in-house Be standard (Braucher *et al.* 2015), whose assumed isotope ratio is 1.191×10^{11}. Correction for a full process blank ratio of $^{10}Be/^{9}Be = 5.4 \pm 0.6 \times 10^{-15}$ was applied.

Surface-exposure ages were computed with the online CREp program (Martin *et al.* 2017; https://crep.otelo.univ-lorraine.fr/#/init). Calculations were performed using a ^{10}Be production rate by neutron spallation at sea level and high latitude (SLHL) of 4.16 ± 0.10 at g^{-1} a^{-1} (Claude *et al.* 2014) scaled at the sample sites using the LSDn scaling scheme (Lifton *et al.* 2014). The ERA-40 reanalysis data set (Uppala *et al.* 2005) and the Lifton-VDM2016 geomagnetic database (Lifton 2016) were used to correct atmospheric pressure and geomagnetic field fluctuations, respectively. Corrections for topographic shielding based on field measurements were also applied (Dunne *et al.* 1999). For assessing the effect of potential post-depositional surface covering (e.g. snow) or surface degradation processes, two end-member scenarios were considered: one without any post-depositional correction and one including snow-cover and surface-erosion corrections. For surface-erosion correction, an erosion rate of 1 mm ka^{-1} was applied, following the argument of Wirsig *et al.* (2016b). The snow-cover correction factor was computed for all boulders following eq. (3.76) in Gosse & Phillips (2001), considering 6 months per year persistence of a 50-cm thick snow cover (Wirsig *et al.* 2016b), a snow density of 0.3 g cm^{-3} and a spallation attenuation length in snow of 109 g cm^{-2} (Delunel *et al.* 2014).

Results

Geomorphological and sedimentological field investigation

We present an updated map of superficial deposits in Fig. 2, showing the Quaternary deposits occurring in the study area and the location of the three study sites (ARP, CRE and SAN).

Accepted Manuscript published at Boreas
(doi.org/10.1111/bor.12480)

Sedimentlogical observations for ARP and CRE deposits are summarised in the stratigraphic logs showed in Figs 4 and 5, respectively (detailed descriptions are given in Tables S3 and S4). The stratigraphy of the ARP deposit (Fig. 4, Table S3) consists of two sediment units lying on top of non-weathered siliceous-limestone bedrock. The 10-cm thick top unit (unit 1) is clast-supported, with siliceous-limestone fragments in a silty matrix. The 30-cm thick basal unit (unit 2) consists of a silty layer with a well-developed platy structure, containing few siliceous-limestone fragments.

The stratigraphy of the CRE alluvial fan (Fig. 5, Table S4) displays the current soil horizon (unit 1) and the recent (i.e. Holocene) coarse alluvial fan deposit (unit 2) in the first 1.5 m of depth. Underneath, a succession of three categories of sediment units can be observed: homogenous clayey silt (units 6, 7, 9, 10, 17, called "fine layers" hereafter), silty clay or loam containing weathered granules and pebbles (units 3, 4, 5, 8, 11, 12, 13, 15, 19, called "heterogeneous layers" hereafter), and gravel layers clast-supported with imbricated elements (units 14, 16, 18).

Grain-size and micromorphology

Grain-size distributions (Fig. 6) show strong similarities between the ARP silty unit (unit 2, samples G7 and G8), and the CRE fine (units 6, 10, 17, samples G2, G3 and G6) and heterogeneous (units 5, 12, 15, samples G1, G4 and G5) layers. Frequency curves are multi-modal and characterised by one primary peak around 35 μm (coarse silt), a secondary peak around 4-8 μm (fine/very fine silt), and a minor peak around 150 μm (fine sand). An additional minor peak around 10^4 μm (pebble) is also visible for samples G4 (CRE site, heterogeneous layer) and G8 (ARP site), which reflects the presence of some isolated clasts as observed in the

stratigraphy (Figs 4, 5). Median grainsize values (D_{50}) range between 11 and 16 μm (fine silt). Calculated So vary between 2.7 and 3.4, reflecting good sorting (with the exception of G4 and G8 which have a So of 5.5 and 4.5 respectively, but reduced to 3.3 and 2.9 if only the clayey, silty and sandy fractions are considered).

Fig. 7 highlights the main micromorphological features observed in thin sections from the CRE alluvial fan. Thin section M1 (fine unit 6; Fig. 7A) displays a moderately-developed sub-angular blocky microstructure in the clayey silt, expressed by slickensides associated with mottling. A low proportion (<2%) of small lithic fragments (<2 mm; not visible in Fig. 7A but similar to the one shown in Fig. 7C) containing quartz grains (20 to 300 μm size) is also recognized. In thin section M2 (fine unit 7; Fig. 7B) and M3 (heterogeneous unit 13), well-developed horizontal laminae (1 to 5-mm thick) with normal grading are observed. In addition, the lower part of thin section M2 (heterogeneous unit 8; not visible in Fig. 7B) contains a higher proportion (5-10%) of weathered (partly-decarbonated) lithic fragments (2-5 mm) in a clayey-silty matrix. Thin section M3 (heterogeneous units 12 and 13; only unit 13 shown in Fig. 7C) shows 40% of weathered (partly- to completely-decarbonated) lithic fragments (3-10 mm) containing quartz grains (20 to 150 μm size), which are embedded in a clayey-silty carbonated matrix. These fragments present different weathering stages, but no weathering cortex on their edges. Lastly, bedrock thin sections display quartz grains of 10 to 150 μm size (the main population ranging between 30 and 50 μm), representing 5-15% of the siliceous limestone and 15-30% of the calcareous shales (Fig. 7D).

X-Ray diffraction and geochemistry

XRD results show four distinct average mineralogical compositions (Fig. 8). Bedrock samples (samples L1-L2 and S1-S2) present similar composition, largely dominated by carbonates (55-66% calcite and up to 5% dolomite). Silicates are secondary components, mainly represented by quartz (23-33%) and micas (3-16%), with some chlorite appearing only in the calcareous shales (S1-S2, up to 4%). ARP sediment samples (ARP01 and ARP03) are carbonate-free and contain 67-70% of quartz and 19% of micas as main components (with up to 8% of chlorite and 4-7% of albite). For CRE samples, two main groups can be distinguished from the mineralogical compositions. Nine samples (CRE02, 03, and 05 to 11) are carbonate-free and contain mainly quartz (40-54%), micas (36-52%) and chlorite (1-14%). The seven other samples (CRE01, 04, and 12 to 16) are characterized by variable calcite content (5-39%), in addition to quartz (32-43%), micas (23-43%) and chlorite (6-11%) components. CRE04 also contains a small percentage of albite (11%), as found in the ARP samples. Geochemistry analyses result in low TOC percentages for all the CRE (0.3-1.2%) and ARP (0.8 and 1.2%) samples.

Geochronology

Portable OSL measurements. ARP and CRE depth-profiles for luminescence signal-intensity are shown in Fig. 9 (samples arp01-arp05) and Fig. 10 (samples cre01-cre16), respectively (luminescence counts are reported in Table S5). For ARP site (Fig. 9), both the quartz OSL and feldspar IRSL intensity profiles could be measured, with more than one order of magnitude difference between OSL (10^3-10^4 counts) and IRSL (10^1-10^2 counts) signals. While the IRSL counts increase consistently with depth (Fig. 9B), the OSL intensity profile is more complex: sample arp03 displays large uncertainty due to the significant difference between the two

358 replicate measurements, and sample arp05 deviates significantly from the increasing-signal trend
359 with depth (Fig. 9A).

360 For CRE site, the general low-feldspar content in the analysed sediments, as highlighted
361 by XRD-analyses (Fig. 8), prevented the measurement of IRSL signal along the section, and only
362 an OSL profile could be obtained (Fig. 10). The measured profile does not follow a stratigraphic
363 coherence (i.e. luminescence signal intensity increasing with depth), but alternates between two
364 signal-intensity groups characterised by low (20-25x10^3 counts) and high (30-50x10^3 counts)
365 OSL counts. These two groups correspond respectively to fine (low signal intensities) and
366 heterogeneous (high signal intensities) layers (Fig. 10).

367

368 Conventional OSL dating. Sample specific information and results, including D_e values, relevant
369 dose-rate data and final CAM ages (Galbraith & Roberts 2012), are shown in Tables 1 and 2, and
370 Figs 9 and 10. Both OSL and IRSL ages were obtained for two ARP samples (ARP01 and
371 ARP02; Fig. 9), while only an IRSL age was measured for sample ARP03 (due to the lack of
372 material for quartz purification). ARP final IRSL and OSL ages range between 2.5 and 7 ka, with
373 high variability between samples and signals despite sample collection at relatively similar
374 depths within unit 2 (25-cm deep; Fig. 4). For both ARP01 and ARP02, the IRSL and OSL
375 ages appear to differ without any systematics (i.e. younger IRSL age for ARP01, the opposite for
376 ARP02).

377 Quartz OSL data for CRE site (Fig. 10) results in two age populations. The first age
378 population concentrates around 11 ka (weighted-average age of 10.5±1.6 ka) and correspond to
379 samples CRE01 (10.0±0.6 ka), CRE02 (12.3±0.7 ka) and CRE04 (9.1±0.6 ka). All three samples

have been collected from fine layers (unit 6 for samples CRE01 and CRE02, unit 17 for sample CRE04). A significantly older age of 27.2±1.1 ka was obtained from sample CRE03, coming from a heterogeneous layer containing pebbles (unit 11). No post-IR IRSL measurements were performed on CRE samples due to the absence of feldspar IRSL signal.

^{10}Be surface exposure dating**.** Sample specific information, as well as measured ^{10}Be concentrations and calculated exposure ages (with and without erosion and snow corrections), are summarized in Table 3 and Fig. 11. A high consistency of the ^{10}Be exposure ages obtained for the three SAN sandstone boulders is evident (9.3±0.4, 9.4±0.4 and 9.8±0.4 ka, without snow and erosion corrections). The three boulder ages agree within uncertainty and yield a weighted-average age estimates of 9.5±0.3 ka (no snow and erosion correction) and 10.3±0.3 ka (with snow and erosion correction).

Discussion

Landform and sediment (post-)depositional histories

High-elevation platform (ARP). Field stratigraphic observations (Table S3) and the different results obtained from the multi-method approach suggest (i) that the silty sediments (unit 2) from the ARP high-elevation platform correspond to an aeolian deposit covered by *in situ* produced cryoclasts (i.e. bedrock limestone clasts derived from freeze and thaw cycles), and (ii) that the whole deposit has been reworked by recent (possibly still ongoing) cryoturbation.

Excluding the coarser grain-size fraction (>2 mm, most probably deriving from isolated cryoclasts) from G7 and G8 grain-size analyses (Fig. 6), the good sorting indexes (2.5 and 3.3 respectively) and the dominance of the silty fraction (D_{50} = 10.1 and 11.1 μm respectively) point

403 towards loess deposit (*sensu stricto*; Pye 1987; Smalley 1995; Muhs 2013). The multi-modal
404 grain-size distributions further suggest a local deflation source, with three main modes (4-8, 35
405 and 150 μm; Fig. 6) roughly corresponding to silicate fractions (micas and quartz) from local
406 bedrock (10-150 μm; Fig. 7D). Observed Lateglacial aeolian deposits at low-elevations in the
407 Rhône Valley (Sion and Bex; Fig. 1) show unimodal grainsize distributions (main mode between
408 20 and 150 μm), very good sorting (1.8) and D_{50} of 35-45 μm (Guélat 2013; and pers. comm.
409 2016). We interpret the different grain-size characteristics between ARP and Rhône Valley loess
410 as the result of a mixed provenance with both local and allochtonous input for ARP deposit.
411 Several arguments allow us to exclude the hypothesis that the ARP silty sediments derive
412 from *in situ* weathering of the underlying siliceous limestone (L1-L2; Fig. 8): (i) the sharp (with
413 no weathering) contact between the base of the ARP aeolian deposit and the underlying bedrock,
414 (ii) the complete absence of carbonates, and (iii) the presence of albite in ARP samples (ARP01
415 and ARP03; Fig. 8). The albite content (4-7%) supports the hypothesis of an allochtonous
416 component within the ARP aeolian deposit, possibly related to the Rhône Valley loess at lower
417 elevations, which is dominated by quartz, micas, chlorite and feldspar mineralogy (Spaltenstein
418 1984; M. Guélat pers. comm. 2016). Such a loessic input was indeed highlighted in a nearby soil
419 profile located 1.7 km south of the Sanetsch Pass (Spaltenstein 1985). However, XRD analyses
420 alone cannot discriminate the dominant source area(s) between Alpine or more distal origin (e.g.
421 Martignier *et al.* 2015) for the ARP aeolian material. Further geochemical analyses would be
422 necessary (Újvári *et al.* 2015) to quantitatively discuss the origin of such aeolian sediments in the
423 context of atmospheric palaeo-circulations at the scale of the European Alps (e.g. Muhs *et al.*
424 2014; Rousseau *et al.* 2018).

Accepted Manuscript published at Boreas
(doi.org/10.1111/bor.12480)

Conventional luminescence dating on ARP silty sediments provides ages ranging between 2 and 7 ka, with an observed discrepancy between OSL and IRSL ages and no clear systematics (Fig. 9, Tables 1, 2). This mismatch is further highlighted by portable luminescence measurements, with different patterns in OSL and IRSL intensity profiles (i.e. higher OSL variability compared to depth-increasing IRSL signal; Fig. 9). Different luminescence signal resetting rates under light exposure (i.e. bleaching) have been reported in the literature (Murray *et al.* 2012), with quartz OSL signal bleaching more rapidly than feldspar IRSL. Our observations can be explained by (i) partial bleaching of the ARP silt before deposition, which would lead to overestimation of the true depositional age, and/or (ii) differential post-depositional bleaching through cryoturbation, which would cause underestimation of the true depositional age. Based on the sedimentology, we favour the post-depositional bleaching hypothesis: there is high probability that the ARP silt was completely bleached prior to deposition, since aeolian sediment transport is commonly associated with efficient sunlight exposure (Li & Wintle 1992). After deposition, active cryoturbation processes resulted in both sediment reworking and formation of the overlying patterned ground (unit 1; Fig. 4). Frost and thaw processes have continually mobilized sediment patches from various depths (Bertran *et al.* 2019), causing light exposure of reworked sediments and the (partial) resetting of their luminescence signal. Similarly, stratigraphic inconsistency and large variability in luminescence ages have been observed for periglacial sediment deposits, and have been attributed to post-depositional reworking due to active cryoturbation processes (Bateman 2008; Andrieux *et al.* 2018). Our young OSL (2.3-4.1 ka) and IRSL (2.5-2.8 ka) ages are therefore probably the result of recent/ongoing post-depositional bleaching through periglacial sediment reworking, while the IRSL age of sample ARP02 (7.1±0.7 ka) is interpreted as minimum age for the high-elevation aeolian deposit. This

minimum age estimate is in agreement with low-elevation loess from the Rhône Valley attributed to the late YD/Early Holocene, based on luminescence dating (Guélat 2013; Parriaux *et al.* 2017).

To summarize, the high-elevation ARP deposit reflects Lateglacial to Holocene aeolian dynamics in the Sanetsch area, in line with previous aeolian sediment reconstructions in the Swiss Alps and foreland (Pochon 1973; Guélat 2013; Martignier *et al.* 2015). The ARP primary aeolian deposit presents a mixed autochthonous (bedrock and moraine-deposit deflation) and allochtonous (nearby alluvial plains such as the Rhône Valley) origin. Luminescence dating suggests that deposition occurred at least *c.* 7 ka ago, however this only remains a minimum age estimate due to recent/ongoing active cryoturbation and sediment reworking at the ARP site. The ARP aeolian deposit may give also insights into the presence of high-elevation ice-free areas (nunataks) in the Alps already during the LGM or the early Lateglacial (Bini *et al.* 2009; Martignier *et al.* 2015; Gild *et al.* 2018), where aeolian sediment could accumulate, in proximity of glacially-covered areas. Furthermore, luminescence analyses (both portable and conventional dating) have highlighted the occurrence of (ongoing) cryoturbation processes at the ARP site, providing potential palaeoclimatic proxy for the Holocene but requiring further investigation (e.g. Vandenberghe 2013; Rousseau *et al.* 2018).

Alluvial fan (CRE site). Insights into the depositional history of the CRE alluvial fan and its connection to the surrounding landforms and deposits also emerge from our multi-method results. XRD and micromorphological analyses confirm field stratigraphic observations (Table S4), revealing a local bedrock origin for the clasts contained in the heterogeneous and gravel layers of the fan (Figs 5, 7, 8). This is suggested by the moderate calcite content (5-39%; Fig. 8)

Accepted Manuscript published at Boreas
(doi.org/10.1111/bor.12480)

in most of the heterogeneous CRE units, which likely relates to the presence of bedrock-derived weathered granules and pebbles (55-66% calcite content in both siliceous limestone and calcareous shales; Fig. 8). The absence of calcite in some heterogeneous layers can be explained by clast weathering and complete decarbonation as observed in the field (very little/no reaction to HCl; Table S4). Thin-section analyses further highlight mineralogical and grain-size similarities between weathered clasts and bedrock (Figs 7C, D), with abundant quartz grains of similar sizes (10-150 μm) in both bedrock and clasts. The absence of a developed weathering cortex around the clasts suggests that weathering did not occur *in situ* (i.e. after clast deposition in the alluvial fan), but is probably inherited from a previous alteration phase (e.g. within morainic and/or slope parental deposits). Further support to this hypothesis is given by the low TOC along the fan stratigraphy, which implies absence of paleo-soils and therefore little *in situ* weathering by pedogenesis.

Field stratigraphic observations, grain-size and XRD analyses also show similarities between the fine/heterogeneous CRE layers and the high-elevation ARP deposit. Grainsize distributions closely overlap for CRE and ARP samples (G1 to G6, and G7 and G8, respectively; Fig. 6), with multiple modes (4-8, 35 and 150 μm), good sorting (2.7-3.3) and silty-fraction dominance (D_{50} between 10.9 and 16.5 μm). Mineralogical analyses further support this observation, with the absence of calcite (except for CRE15, which probably integrates clasts from overlying/underlying gravel units) and the dominance of quartz (40-54%) and micas (23-43%). Stratigraphy and micromorphological analyses also show (i) fining-up sedimentary sequences within some CRE units (i.e. from weathered calcareous granules and pebbles at the base to silty loam at the top; Fig. 5, Table S4), (ii) a moderately-developed sub-angular blocky microstructure (unit 6; Fig. 7A) and (iii) well-developed 1 to 5-mm thick horizontal laminae

Accepted Manuscript published at Boreas
(doi.org/10.1111/bor.12480)

(units 7 and 13; Fig. 7B). All together, these observations point towards an alluvial reworking of aeolian sediments to form the fine units and the matrix of the heterogeneous units of the CRE alluvial fan. Deposition of reworked aeolian sediments could have occurred in a lake, or possibly in a pond within the alluvial fan, as suggested by the fining-up sedimentary sequences (units 3, 4 and 5) and the horizontal laminae (units 7 and 13). Isolated pebbles and cobbles (fine units 7, 9 and 10) can be interpreted as possible dropstones, and would support the lake hypothesis. Based on the presence of slickensides and mottling (unit 6; Fig. 7A) as well as Fe-Mn precipitation, we hypothesize ephemeral lake/pond conditions with wetting/drying cycles and low-sedimentation phases, during which the original depositional microstructure (Fig. 7B) was destroyed.

Luminescence measurements (both portable and conventional OSL), show a general alternating pattern between two populations of low-counts/young-ages and high-counts/old-age along the fan stratigraphy (Fig. 10). We propose that these OSL trends reflect differences in quartz provenance as well as transport processes. For the heterogeneous layers, we expect the high OSL counts and old OSL age to result from the mixing and signal-averaging between grains from weathered clasts carrying an inherited signal (i.e. no-light exposure during transport) with well-bleached grains (i.e. full luminescence signal reset prior deposition) coming from reworked loess material. Moreover, sediments from heterogeneous units were probably transported and deposited during periods of high-sediment supply by sheet flow events: transportation in dense and turbid flows could have prevented the complete OSL bleaching of reworked quartz grains, leading therefore to higher luminescence counts and overestimated OSL age (i.e. CRE03 at 27.2±1.1 ka). Fine layers, characterised by low OSL count and young OSL ages, may have settled during periods of lower sediment supply by decantation in water, allowing complete/better OSL bleaching prior to deposition. We therefore interpret OSL ages of the fine

CRE units (CRE01, 02 and 04; weighted-average age of 10.5±1.6 ka) as more representative of the true depositional age of the CRE alluvial fan. Potential incorporation of lithic fragments could explain the slightly older OSL age for sample CRE02 (12.3±1.6 ka, unit 6). In summary, CRE fan deposition most likely occurred during or soon after the YD. This proposed chronology agrees with the onset of sedimentation in Pond Emine (Fig. 2) at *c.* 12 ka ago (Berthel *et al.* 2012; Steinemann *et al.* 2020), implying that the Sanetsch Pass and the alluvial plain were ice free during (or soon after) the YD, and that the subsequent sediment connectivity and transport from the hillslopes towards the plain (CRE site) established quickly.

Hummocky moraine and rockfall boulders (SAN site). The average ^{10}Be surface exposure age from the three rockfall boulders is 10.3±0.3 or 9.5±0.2 ka, calculated respectively with or without erosion and snow corrections. For the rest of the discussion, we focus on the age estimate obtained with erosion (1 mm ka^{-1}; Wirsig *et al.* 2016b) and snow corrections (50-cm snow thickness over 6 month per year; based on Wirsig *et al.* 2016b and our own field observations). We however note that uncorrected age estimate differs by <10%, and would not lead to any significant change in our proposed geomorphological reconstruction.

Dating of the rockfall boulders (*c.* 10 ka; Fig. 11) provides a minimum age constraint for the hummocky moraine formation, which occurred before or at the time of the rockfall event. Based on field observations of boulder distribution, we propose a scenario where the rockfall occurred over stagnant ice. If the rockfall had occurred when the hummocky moraine was already formed, the boulders would have been deposited mainly in the intra-hummock hollows, due to gravity. Instead, the uniform distribution of rockfall boulders, placed both on hummock ridges and in intra-hummock hollows, suggests that the rockfall spread over a disconnected ice

Accepted Manuscript published at Boreas
(doi.org/10.1111/bor.12480)

body, before or during the formation of the underlying hummocky morphology. We further hypothesise that this stagnant ice body could have temporally dammed an ephemeral lake in the plain, where the CRE alluvial fan was deposited around 10 ka ago.

At a regional scale, this rockfall event is contemporaneous with several other Early Holocene gravitational events reported within the Alps (10-9 ka; Ivy-Ochs *et al.* 2017 and reference therein), including two coeval landslides of the Rinderhorn region (Bernese Alps, Switzerland; Grämiger *et al.* 2016), at only 28-km distance from the Sanetsch Pass. Glacial debuttressing (Cossart *et al.* 2008) and rock stress changes associated with repeated glacial fluctuations (Grämiger *et al.* 2017) were probably the trigger mechanisms behind the rockslope failure.

The rockfall event investigated here was probably followed by a second event, characterized by smaller extent (Fig. 11). Age constraint for this subsequent event is however not available, but may be related to Holocene landslide/rockslide clusters observed elsewhere in the European Alps (Zerathe *et al.* 2014; Ivy-Ochs *et al.* 2017).

Lateglacial to Holocene palaeoenvironmental reconstruction

By combining our field observations and multi-method results, we propose a palaeoenvironmental reconstruction of the Sanetsch Pass area during the Lateglacial-Holocene transition, with the aim to highlight the interplay between different sedimentary and geomorphic processes (Fig. 12).

Throughout the LGM and Lateglacial periods, the area north of Sanetsch Pass was ice-covered, while some peaks were protruding above the ice surface (nunataks, Fig. 12A; Bini *et al.* 2009), similar to the overall European Alps. These conditions may have favoured deposition of

563 aeolian drapes on nunatak platforms already at that time (Gild *et al.* 2018), with an allochtonous
564 contribution of the wind-blown material as confirmed by XRD analyses (ARP site), although
565 local *vs.* more distal sources cannot be discriminated by our multi-method approach and would
566 require further investigations. Lateral morainic ridges and glacial deposits in the Sanetsch plain
567 (Fig. 2) do not have tight chronological constraints but they are likely related to ice retreat
568 stadials during the Lateglacial (Ivy-Ochs *et al.* 2007). Several indications point towards an onset
569 of glacier retreat for the Sanetsch Pass and our investigated area at the end of the YD (Fig. 12B),
570 in close agreement with other palaeo-glacial and lacustrine chronologies in the Swiss Alps
571 (Schwander *et al.* 2000; Heiri *et al.* 2014; Schimmelpfennig *et al.* 2014). The Pond Emines (Fig.
572 2) became ice-free during the same time period (*c.* 12 ka; Berthel *et al.* 2012), when the
573 Tsanfleuron glacier finally retreated close to the most external LIA morainic ridges (□ 1 km
574 west of the Sanetsch Pass; Fig. 2), similar to other palaeo-glaciological reconstructions in the
575 Alps (Schimmelpfennig *et al.* 2012; Kronig *et al.* 2018). A disconnected ice body, thick and
576 sediment rich, persisted at the downstream end of the Sanetsch plain until *c.* 10 ka and formed a
577 hummocky morphology overridden by rockfall deposits.

578 Glacier retreat in the Sanetsch Pass area was associated with rapid (re-)establishment of
579 paraglacial and periglacial geomorphic processes, promoting sediment connectivity and
580 transport, resulting in major landscape changes. All these processes illustrate and synthesize
581 post-glacial alpine dynamics (Church & Ryder 1972; Mercier & Etienne 2008; Fig. 12B), as
582 summarized below. Firstly, ice retreat promoted slope processes, as well as aeolian
583 remobilization of glacially-derived erosion products. Fine sediments in glacial outwash plains,
584 within the Sanetsch Pass area or other nearby valleys (e.g. the Rhône Valley), were probably
585 entrained and redeposited on mountain flanks and low-relief areas by local katabatic winds

and/or regional winds (Bullard & Austin 2011; Martignier *et al.* 2015). Post-YD paraglacial relaxation favoured hillslope dynamics and sediment entrainment (Sanders & Ostermann, 2011), with catastrophic rockfall events such as the rockslope failure of Les Montons cliff (Figs 3, 11; Ivy-Ochs *et al.* 2017). The alluvial fan (CRE site) was deposited at the downstream end of the fluvioglacial plain, probably within an ephemeral ice-dammed lake contemporary to the hummocky moraine formation. Exposed catchment-slope deposits (i.e. aeolian, glacial and talus) were remobilized and transported downhill into the plain, where they were redeposited to form a stratigraphic succession of coarse and fine layers within the CRE alluvial fan (Beaudoin & King 1994). We propose that the aeolian deposit identified on the high-elevation plateau (ARP site) is a remnant of a broader aeolian drape. The ARP aeolian sediments have been preserved due to the low connectivity between the platform and the downstream hillslopes (Figs 2, 3), but this potentially more-extensive deposit has been eroded elsewhere in the Sanetsch Pass area, with the reworked fine sediments being eventually incorporated in the alluvial fan downslope.

Based on our OSL chronology, we hypothesize that short-lived sedimentation in the CRE alluvial fan stopped or slowed down already during/soon after the YD, resulting from a drastic change in base-level and sedimentation dynamics due to the melting of the ice-dam. Since then, landscape dynamics around the Sanetsch Pass seem to have been dominated by (i) hillslope denudation and localized stream incision within bedrock and glacial/alluvial sediments (Figs 2, 3C) at low elevations, and (ii) active periglacial processes at high elevations, with aeolian-sediment cryoturbation (ARP site) and rock glaciers within scree deposits (Fig. 2).

Conclusions

608 Based on a combined approach of geomorphological and sedimentological field investigations
609 together with different analytical methods, we proposed a detailed reconstruction of post-LGM
610 palaeoenvironmental conditions and geomorphic connectivity in the Sanetsch Pass area (western
611 Swiss Alps). Our study brings quantitative constraints on the high-altitude landscape response to
612 ice retreat and climate changes during the Lateglacial-Holocene transition. Our multi-method
613 results show that silty sediments from the high-elevation platform are primary aeolian sediments,
614 deposited on ice-free areas before or at the post-YD glacier retreat and then reworked by
615 cryoturbation. Post-YD ice retreat was also associated with slope relaxation and aeolian/glacial
616 sediment remobilization. This is evidenced by the contemporary occurrence of hummocky
617 moraine formation, rockfall event and alluvial fan deposition within an ephemeral ice-dammed
618 lake, all taking place at *c.* 10-12 ka. Altogether, our results highlight the development of rapid
619 and most probably transient landscape changes in high Alpine regions during the Lateglacial-
620 Holocene transition, with an increase in sediment flux following glacier retreat and the
621 establishment of paraglacial and periglacial geomorphic processes.

622 Several palaeoclimatic archives, mainly from lacustrine and peat records, have
623 documented the pronounced climatic and environmental change associated with the end of the
624 YD in the European Alps. In this study, we have shown that landscape dynamics and
625 connectivity between geomorphic markers can also be used as quantitative proxies to constrain
626 the environmental response to such climatic transition.

627

628 Acknowledgements. The authors thank M. Gobat for sharing his intuition of a possible aeolian
629 deposit on the Arpille plateau, and N. Diaz, P. Pérez Cutillas and B. Lehmann for help during
630 field investigations. S. Lane (University of Lausanne) is warmly thanked for access to the

portable luminescence reader. P. Renzel and T. Beckmann are thanked for the grainsize analyses and micromorphological thin-section preparation. M. Guélat is thanked for sharing unpublished mineralogical and grainsize data from aeolian deposits of the Rhône Valley. J. Krbanjevic is thanked for support during geochemistry analyses. The authors warmly thank the ASTER team (D. Bourlès, G. Aumaitre, K. Keddadouche, and R. Braucher) for the measurements performed at the ASTER AMS facility (CEREGE, Aix-en-Provence). I. Schimmelpfening, one anonymous reviewer, and the editor J. Piotrowski are thanked for constructive reviews and manuscript corrections. This study was supported by the Swiss National Science Foundation SNSF (Grant PP00P2_170559) and the French ANR-PIA programme (ANR-18- MPGA-0006). All data are available in tables in the main text and online supporting information.

Author contributions. LB, PGV, and RD designed the study; ES, LB, PGV, and RD performed field investigations and sample collection. ES performed luminescence analysis (with NG and PGV), grainsize and micromorphology (with LB), XRD analysis (with BG), and ^{10}Be cosmogenic analysis (with JC and PGV). ES wrote the manuscript with input from all co-authors.

References

Aitken, M. J. 1985: Thermoluminescence dating: Past progress and future trends. *Nuclear Tracks and Radiation Measurements (1982) 10*, 3–6.

Andrieux, E., Bateman, M. D. & Bertran, P. 2018: The chronology of Late Pleistocene thermal contraction cracking derived from sand wedge OSL dating in central and southern France. *Global and Planetary Change 162*, 84-100.

Arnold, M., Merchel, S., Bourlès, D. L., Braucher, R., Benedetti, L., Finkel, R. C., Aumaître, G., Gottdang, A. & Klein, M. 2010: The French accelerator mass spectrometry facility ASTER: Improved performance and developments. *Nuclear Instruments and Methods in Physics Research Section B: Beam Interactions with Materials and Atoms 268*, 1954–1959.

Auclair, M., Lamothe, M. & Huot, S. 2003: Measurement of anomalous fading for feldspar IRSL using SAR. *Radiation Measurements 37*, 487–492.

Badoux, H., Bonnard, E. G., Burri, M. & Vischer, A. 1959: *Map sheet 1286 St-Léonard with explanatory note 35. Swiss Geological Atlas 1:25000.*

Ballantyne, C. K. 2002: Paraglacial geomorphology. *Quaternary Science Reviews 21*, 1935–2017.

Bateman, M. D. 2008: Luminescence dating of periglacial sediments and structures. *Boreas 37*, 574-588.

Beaudoin, A. B. & King, R. H. 1994: Holocene palaeoenvironmental record preserved in a paraglacial alluvial fan, Sunwapta Pass, Jasper National Park, Alberta, Canada. *Catena 22*, 227–248.

Benn, D. I. & Evans, D. J. A. 2014: *Glaciers and Glaciation.* 259-568 pp. Routledge, London.

Berthel, N., Schwörer, C. & Tinner, W. 2012: Impact of Holocene climate changes on alpine and treeline vegetation at Sanetsch Pass, Bernese Alps, Switzerland. *Review of Palaeobotany and Palynology 174*, 91–100.

Bertran, P., Font, M., Giret, A., Manchuel, K. & Sicilia, D. 2019: Experimental soft-sediment deformation caused by fluidization and intrusive ice melt in sand. *Sedimentology 66*, 1102–1117.

Bini, A., Buoncristiani, J., Couterrand, S. & Ellwanger, D. 2009: *Switzerland during the Last Glacial Maximum (LGM) 1: 500000.* Federal Office of Topography, Swisstopo.

Borgatti, L. & Soldati, M. 2010: Landslides as a geomorphological proxy for climate change: A record from the Dolomites (northern Italy). *Geomorphology 120*, 56–64.

Braucher, R., Guillou, V., Bourles, D.L., Arnold, M., Aumaitre G., Keddadouche, K. & E. Nottoli 2015: Preparation of ASTER in-house $^{10}Be/^{9}Be$ standard solutions. *Nuclear Instruments and Methods in Physics Research Section B*: *Beam Interactions with Materials and Atoms 361*, 335-340.

679 Brown, E. T., Edmond, J.M., Raisbeck, G. M., Yiou, F., Kurz, M. D. & Brook, E. J. 1991: Examination
680 of surface exposure ages of Antarctic moraines using in situ produced ^{10}Be and ^{26}Al. *Geochimica*
681 *et Cosmochimica Acta 55*, 2269–2283.
682 Bullard, J. E. & Austin, M. J. 2011: Dust generation on a proglacial floodplain, West Greenland. *Aeolian*
683 *Research 3*, 43–54.
684 Buylaert, J. P., Murray, A. S., Thomsen, K. J. & Jain, M. 2009: Testing the potential of an elevated
685 temperature IRSL signal from K-feldspar. *Radiation Measurements 44*, 560–565.
686 Church, M. & Ryder, J. M. 1972: Paraglacial sedimentation: A consideration of fluvial processes
687 conditioned by glaciation. *Bulletin of the Geological Society of America 83*, 3059–3072.
688 Clark, P. U., Dyke, A. S., Shakun, J. D., Carlson, A. E., Clark, J., Wohlfarth, B., Mitrovica, J. X.,
689 Hostetler, S. W. & McCabe, A. M. 2009: The Last Glacial Maximum. *Science 325*, 710–4.
690 Claude, A., Ivy-Ochs, S., Kober, F., Antognini, M., Salcher, B. & Kubik, P. W. 2014: The Chironico
691 landslide (Valle Leventina, southern Swiss Alps): age and evolution. *Swiss Journal of*
692 *Geosciences 107*, 273–291.
693 Colombo, N., Paro, L., Godone, D. & Fratianni, S. 2016: Geomorphology of the Hohsand basin (Western
694 Italian Alps). *Journal of Maps 12*, 975–978.
695 Cossart, E., Braucher, R., Fort, M., Bourlès, D. L. & Carcaillet, J. 2008: Slope instability in relation to
696 glacial debuttressing in alpine areas (Upper Durance catchment, southeastern France): Evidence
697 from field data and ^{10}Be cosmic ray exposure ages. *Geomorphology 95*, 3–26.
698 Cossart, E., Mercier, D., Decaulne, A. & Feuillet, T. 2013: An overview of the consequences of
699 paraglacial landsliding on deglaciated mountain slopes: typology, timing and contribution to
700 cascading fluxes. *Quaternaire 24,* 13–24.
701 Delunel, R., Bourlès, D. L., van der Beek, P. A., Schlunegger, F., Leya, I., Masarik, J. & Paquet, E. 2014:
702 Snow shielding factors for cosmogenic nuclide dating inferred from long-term neutron detector
703 monitoring. *Quaternary Geochronology 24*, 16–26.

Dunne, J., Elmore, D. & Muzikar, P. 1999: Scaling factors for the rates of production of cosmogenic nuclides for geometric shielding and attenuation at depth on sloped surfaces. *Geomorphology 27*, 3–11.

Durcan, J. A., King, G. E. & Duller, G. A. T. 2015: DRAC: Dose Rate and Age Calculator for trapped charge dating. *Quaternary Geochronology 28*, 54–61.

Ehlers, J. & Gibbard, P. 2004: *Quaternary Glaciations-Extent and Chronology: part I: Europe*. Elsevier, Amsterdam.

Föllmi, K. B., Bodin, S., Godet, A., Linder, P. & van de Schootbrugge, B. 2007: Unlocking paleo-environmental information from Early Cretaceous shelf sediments in the Helvetic Alps: stratigraphy is the key! *Swiss Journal of Geosciences 100*, 349–369.

French, H. M. 2007: *The Periglacial Environment*. 116-151 pp. John Wiley & Sons, Chichester.

Galbraith, R. F. & Roberts, R. G. 2012: Statistical aspects of equivalent dose and error calculation and display in OSL dating: An overview and some recommendations. *Quaternary Geochronology 11*, 1–27.

Geilhausen, M., Morche, D., Otto, J. -C. & Schrott, L. 2013: Sediment discharge from the proglacial zone of a retreating Alpine glacier. *Zeitschrift für Geomorphologie, Supplementary Issues 57*, 29–53.

Gild, C., Geitner, C. & Sanders, D. 2018: Discovery of a landscape-wide drape of Lateglacial aeolian silt in the western Northern Calcareous Alps (Austria): First results and implications. *Geomorphology 301*, 39–52.

Gobat, J. & Guenat, C. 2019: *Sols et paysages. Types de sols, fonctions et usages en Europe moyenne*. 158-169 pp. PPUR, Lausanne.

Gosse, J. C. & Phillips, F. M. 2001: Terrestrial in situ cosmogenic nuclides: theory and application. *Quaternary Science Reviews 20*, 1475–1560.

Grämiger, L. M., Moore, J. R., Gischig, V. S., Ivy-Ochs, S. & Loew, S. 2017: Beyond debuttressing: Mechanics of paraglacial rock slope damage during repeat glacial cycles. *Journal of Geophysical*

Research: Earth Surface 122, 1004–1036.

Grämiger, L. M., Moore, J. R., Vockenhuber, C., Aaron, J., Hajdas, I. & Ivy-Ochs, S. 2016: Two early Holocene rock avalanches in the Bernese Alps (Rinderhorn, Switzerland). *Geomorphology 268*, 207–221.

Guélat, M. 2013: Les Loess de la Vallée du Rhône. *Bulletin de la Murithienne 131*, p. 109.

Hadjouis, A. 1987: Granulométrie des fractions sableuses. *Géologie de la préhistoire: méthodes, techniques, applications, sous la direction de JC Miskovsky*. 413-426 pp. AEEGP, Paris.

Hanspeter, H., Michel, M. & Heinz, Z. 2005: Glacier and lake-level variations in west-central Europe over the last 3500 years. *The Holocene 6*, 789–801.

Hantke, R. 1992: *Eiszeitalter - Die jüngste Erdgeschichte der Alpen und ihrer Nachbargebiete.* Ecomed-Verlag, Landsberg/Lech.

Heiri, O., Koinig, K. A., Spötl, C., Barrett, S., Brauer, A., Drescher-Schneider, R., Gaar, D., Ivy-Ochs, S., Kerschner, H., Luetscher, M., Moran, A., Nicolussi, K., Preusser, F., Schmidt, R., Schoeneich, P., Schwörer, C., Sprafke, T., Terhorst, B. & Tinner, W. 2014: Palaeoclimate records 60-8 ka in the Austrian and Swiss Alps and their forelands. *Quaternary Science Reviews 106*, 186–205.

Hinderer, M. 2001: Late Quaternary denudation of the Alps, valley and lake fillings and modern river loads. *Geodinamica Acta 14*, 231–263.

Hippe, K., Ivy-Ochs, S., Kober, F., Zasadni, J., Wieler, R., Wacker, L., Kubik, P. W. & Schlüchter, C. 2014: Chronology of Lateglacial ice flow reorganization and deglaciation in the Gotthard Pass area, Central Swiss Alps, based on cosmogenic ^{10}Be and in situ ^{14}C. *Quaternary Geochronology 19*, 14–26.

Huntley, D. J. & Lamothe, M. 2011: Ubiquity of anomalous fading in K-feldspars and the measurement and correction for it in optical dating. *Canadian Journal of Earth Sciences 38*, 1093–1106.

Ivy-Ochs, S. 2015: Glacier variations in the European Alps at the end of the last glaciation. *Cuadernos de Investigación Geográfica 41*, 295-315.

754 Ivy-Ochs, S., Kerschner, H., Maisch, M., Christl, M., Kubik, P.W. & Schlüchter, C. 2009: Latest
755 Pleistocene and Holocene glacier variations in the European Alps. *Quaternary Science Reviews*
756 *28*, 2137–2149.

757 Ivy-Ochs, S., Kerschner, H. & Schlüchter, C. 2007: Cosmogenic nuclides and the dating of Lateglacial
758 and Early Holocene glacier variations: The Alpine perspective. *Quaternary International 164–*
759 *165*, 53–63.

760 Ivy-Ochs, S., Martin, S., Campedel, P., Hippe, K., Alfimov, V., Vockenhuber, C., Andreotti, E., Carugati,
761 G., Pasqual, D., Rigo, M. & Viganò, A. 2017: Geomorphology and age of the Marocche di Dro
762 rock avalanches (Trentino, Italy). *Quaternary Science Reviews 169*, 188–205.

763 Ivy-Ochs, S., Schäfer, J., Kubik, P. W., Synal, H. A. & Schlüchter, C. 2004: Timing of deglaciation on
764 the northern Alpine foreland (Switzerland). *Eclogae Geologicae Helvetiae 97*, 47–55.

765 King, G. E., Sanderson, D. C. W., Robinson, R. A. J. & Finch, A. A. 2014: Understanding processes of
766 sediment bleaching in glacial settings using a portable OSL reader. *Boreas 43*, 955–972.

767 Korup, O. & Schlunegger, F. 2007: Bedrock landsliding, river incision, and transience of geomorphic
768 hillslope-channel coupling: Evidence from inner gorges in the Swiss Alps. *Journal of*
769 *Geophysical Research: Earth Surface 112*, F03027. https://doi.org/10.1029/2006JF000710

770 Kreutzer, S., Schmidt, C., Fuchs, M. & Dietze, M. 2012: Introducing an R package for luminescence
771 dating analysis. *Ancient TL 30*, 1–8.

772 Kronig, O., Ivy-Ochs, S., Hajdas, I., Christl, M., Wirsig, C. & Schlüchter, C. 2018: Holocene evolution of
773 the Triftje- and the Oberseegletscher (Swiss Alps) constrained with 10Be exposure and
774 radiocarbon dating. *Swiss Journal of Geosciences 111*, 117–131.

775 Li, S.H. & Wintle, A.G. 1992: Luminescence sensitivity change due to bleaching of sediments.
776 *International Journal of Radiation Applications and Instrumentation. Part 20*, 567–573.

777 Lifton, N. 2016: Implications of two Holocene time-dependent geomagnetic models for cosmogenic
778 nuclide production rate scaling. *Earth and Planetary Science Letters 433*, 257–268.

779 Lifton, N., Sato, T. & Dunai, T. J. 2014: Scaling in situ cosmogenic nuclide production rates using
780 analytical approximations to atmospheric cosmic-ray fluxes. *Earth and Planetary Science Letters*
781 *386*, 149–160.
782 Lowick, S. E., Buechi, M. W., Gaar, D., Graf, H. R. & Preusser, F. 2015: Luminescence dating of Middle
783 Pleistocene proglacial deposits from northern Switzerland: methodological aspects and
784 stratigraphical conclusions. *Boreas 44*, 459–482.
785 Martignier, L., Nussbaumer, M., Adatte, T., Gobat, J. M. & Verrecchia, E. P. 2015: Assessment of a
786 locally-sourced loess system in Europe: The Swiss Jura Mountains. *Aeolian Research 18*, 11–21.
787 Martin, L. C. P., Blard, P.- H., Balco, G., Lavé, J., Delunel, R., Lifton, N. & Laurent, V. 2017: The CREp
788 program and the ICE-D production rate calibration database: A fully parameterizable and updated
789 online tool to compute cosmic-ray exposure ages. *Quaternary Geochronology 38*, 25–49.
790 Masson, H., Herb, R. & Steck, A. 1980: Helvetic Alps of Western Switzerland. *Geology of Switzerland, a*
791 *guide book (Part B)*. pp. 109–153. Wepf and Co, Basel.
792 Menkveld-Gfeller, U. 1997: Die Bürgen-Fm. und die Klimsenhorn-Fm.: Formelle Definition zweier
793 lithostratigraphischer Einheiten des Eozäns der helvetischen Decken. *Eclogae Geologicae Helvetiae*
794 *90,* 245-261.
795 Merchel, S. & Herpers, U. 1999: An update on radiochemical separation techniques for the determination
796 of long-lived radionuclides via accelerator mass spectrometry. *Radiochimica Acta 84*, 215-220.
797 Mercier, D. & Etienne, S. 2008: Paraglacial geomorphology: Processes and paraglacial context.
798 *Geomorphology 95*, 1–2.
799 Muhs, D. R. 2013: Loess and its Geomorphic, Stratigraphic, and Paleoclimatic Significance in the
800 Quaternary. In *Treatise on Geomorphology*. Elsevier Inc., 149–183.
801 Muhs, D. R., Cattle, S. R., Crouvi, O., Rousseau, D. D., Sun, J & Zárate, M. A. 2014: Loess record. In:
802 *Mineral Dust: A Key Player in the Earth System*. Springer Netherlands, 411-441.
803 Muñoz-Salinas, E., Bishop, P., Sanderson, D. & Kinnaird, T. 2014: Using OSL to assess hypotheses

related to the impacts of land use change with the early nineteenth century arrival Of europeans in southeastern Australia: An exploratory case study from Grabben Gullen Creek, New South Wales. *Earth Surface Processes and Landforms 39*, 1576–1586.

Murray, A. S. & Wintle, A. G. 2000: Dating quartz using an improved single-aliquot regenerative-dose (SAR) protocol. *Radiation Measurements 32*, 57–73.

Murray, A. S., Thomsen, K. J., Masuda, N., Buylaert, J. P. & Jain, M. 2012: Identifying well-bleached quartz using the different bleaching rates of quartz and feldspar luminescence signals. *Radiation Measurements 47*, 688–695.

Nelson, M. S., Gray, H. J., Johnson, J. A., Rittenour, T. M., Feathers, J. K. & Mahan, S. A. 2015: User Guide for Luminescence Sampling in Archaeological and Geological Contexts. *Advances in Archaeological Practice 3*, 166–177.

Parriaux, A., Burri, M., Weidmann, M. 2017: Données nouvelles sur la géologie des collines de Chiètres. *Bull. de la Société vaudoise des Sci. Nat. 96*, 31–48.

Pochon, M., 1973: Apport allochtone dans les sols jurassiens (Jura vaudois et Jura neuchâtelois). *Bull. Soc. Neuchâtel. Sci. Nat. 96,* 135–147.

Pye, K. 1987: *Aeolian dust and dust deposits*. Academic Press.

Preusser, F. & Kasper, H. U. 2001: Comparison of dose rate determination using high-resolution gamma spectrometry and inductively coupled plasma-mass spectrometry. *Ancient TL 19*, 17–21.

Rasmussen, S. O., Vinther, B. M., Clausen, H.B. & Andersen, K. K. 2007: Early Holocene climate oscillations recorded in three Greenland ice cores. *Quaternary Science Reviews 26*, 1907–1914.

Rietveld, H. M. 1969: A profile refinement method for nuclear and magnetic structures. *Journal of Applied Crystallography 2*, 65–71.

Rivière, A. 1977: *Méthodes granulométriques, techniques et interprétation*. Masson, Paris.

Rolland, Y., Petit, C., Saillard, M., Braucher, R., Bourlès, D., Darnault, R. & Cassol, D. 2017: Inner gorges incision history: A proxy for deglaciation? Insights from Cosmic Ray Exposure dating

(^{10}Be and ^{36}Cl) of river-polished surfaces (Tinée River, SW Alps, France). *Earth and Planetary Science Letters 457*, 271–281.

Rousseau, D. -D., Derbyshire, E., Antoine, P. & Hatté, C. 2018: European loess records. In *Reference Module in Earth System and Environmental Sciences*. Elsevier, Amsterdam. https://doi.org/10.1016/B978-0-12-409548-9.11136-4

Sanders, D. & Ostermann, M. 2011: Post-last glacial alluvial fan and talus slope associations (Northern Calcareous Alps, Austria): A proxy for Late Pleistocene to Holocene climate change. *Geomorphology 131*, 85–97.

Sanderson, D. C. W. & Murphy, S. 2010: Using simple portable OSL measurements and laboratory characterisation to help understand complex and heterogeneous sediment sequences for luminescence dating. *Quaternary Geochronology 5*, 299–305.

Schmidt, R., Weckström, K., Lauterbach, S., Tessadri, R. & Huber, K. 2012: North Atlantic climate impact on early Lateglacial climate oscillations in the south-eastern Alps inferred from a multi-proxy lake sediment record. *Journal of Quaternary Science 27*, 40–50.

Schimmelpfennig, I., Schaefer, J. M., Akçar, N., Ivy-Ochs, S., Finkel, R. C. & Schlüchter, C. 2012: Holocene glacier culminations in the Western Alps and their hemispheric relevance. *Geology 40*, 891–894.

Schimmelpfennig, I., Schaefer, J. M., Akçar, N., Koffman, T., Ivy-Ochs, S., Schwartz, R., Finkel, R. C., Zimmerman, S. & Schlüchter, C. 2014: A chronology of Holocene and Little Ice Age glacier culminations of the Steingletscher, Central Alps, Switzerland, based on high-sensitivity beryllium-10 moraine dating. *Earth and Planetary Science Letters 393*, 220–230.

Schwander, J., Eicher, U. & Ammann, B. 2000: Oxygen isotopes of lake marl at Gerzensee and Leysin (Switzerland), covering the Younger Dryas and two minor oscillations, and their correlation to the GRIP ice core. *Palaeogeography, Palaeoclimatology, Palaeoecology 159*, 203–214.

Smalley, I. J. 1995: Making the material: The formation of silt sized primary mineral particles for loess

deposits. *Quaternary Science Reviews 14*, 645–651.

Spaltenstein, H. 1984: *Pédogenèse sur calcaire dur dans les Hautes Alpes calcaires.* Ph.D. thesis (N°540), Ecole polytechnique fédérale de Lausanne. 540 p.

Spaltenstein, H. 1985: Caractérisation de deux sols alpins minces sur calcaire dur dans le lapiaz du Sanetsch. *Bulletin de la Société vaudoise des sciences naturelles, 77,* 245-254.

Stang, D. M., Rhodes, E. J. & Heimsath, A. M. 2012: Assessing soil mixing processes and rates using a portable OSL-IRSL reader: Preliminary determinations. *Quaternary Geochronology 10*, 314–319.

Steinemann, O., Ivy-Ochs, S., Grazioli, S., Luetscher, M., Fischer, U. H., Vockenhuber, C. & Synal, H. 2020: Quantifying glacial erosion on a limestone bed and the relevance for landscape development in the Alps. *Earth Surface Processes and Landforms 45,*1401-1417.

Toby, B. H. 2006: R factors in Rietveld analysis: How good is good enough?. *Powder diffraction 21*, 67-70.

Uppala, S.M., and others 2005: The ERA-40 re-analysis. *Quarterly Journal of the Royal Meteorological Society 131*, 2961–3012.

Újvári, G., Stevens, T., Svensson, A., Klötzli, U. S., Manning, C., Németh, T., Kovács, J., Sweeney, M. R., Gocke, M., Wiesenberg, G. L. B., Markovic, S. B. & Zech, M. 2015: Two possible source regions for central Greenland last glacial dust. *Geophysical Research Letters 42*, 10399–10408.

Valla, P. G., Van Der Beek, P. A. & Lague, D. 2010: Fluvial incision into bedrock: Insights from morphometric analysis and numerical modeling of gorges incising glacial hanging valleys (Western Alps, France). *Journal of Geophysical Research: Earth Surface 115*, F02010. 10.1029/2008JF001210

Vandenberghe, J. 2013: Cryoturbation Structures. In: *The Encyclopedia of Quaternary Science*, *vol. 3*. 430-435 pp.. Elsevier, Amsterdam.

Wallinga, J., Bos, A. J. J., Dorenbos, P., Murray, A. S. & Schokker, J. 2007: A test case for anomalous fading correction in IRSL dating. *Quaternary Geochronology 2*, 216–221.

879 Wintle, A. G. & Murray, A. S. 2006: A review of quartz optically stimulated luminescence characteristics
880 and their relevance in single-aliquot regeneration dating protocols. *Radiation Measurements 41*,
881 369–391.
882 Wirsig, C., Zasadni, J., Christl, M., Akçar, N. & Ivy-Ochs, S. 2016a: Dating the onset of LGM ice surface
883 lowering in the High Alps. *Quaternary Science Reviews 143*, 37–50.
884 Wirsig, C., Zasadni, J., Ivy-Ochs, S., Christl, M., Kober, F. & Schlüchter, C. 2016b: A deglaciation model
885 of the Oberhasli, Switzerland. *Journal of Quaternary Science 31*, 46–59.
886 Zerathe, S., Lebourg, T., Braucher, R. & Bourlès, D. 2014: Mid-Holocene cluster of large-scale landslides
887 revealed in the Southwestern Alps by ^{36}Cl dating. Insight on an Alpine-scale landslide activity.
888 *Quaternary Science Reviews 90*, 106–127.

Accepted Manuscript published at Boreas
(doi.org/10.1111/bor.12480)

889 **List of Figures**

890 **Figure 1.** Location of the study area (swissALTI3D DEM from swisstopo, authorization
891 5701367467/000010). Present-day glaciers, main peaks around the Sanetsch Pass and the Rhône
892 River are marked. The yellow box indicates the extent of the geomorphological map presented in
893 Fig. 2. Inset shows location of the Sanetsch Pass (red box) within Switzerland and the European
894 Alps, with the LGM ice extent (Ehlers & Gibbard 2004).

895

896 **Figure 2.** Detailed map of the Quaternary deposits occurring in the study area (swissALTI3D
897 DEM from swisstopo, authorization 5701367467/000010). The different Quaternary deposits and
898 the three study sites are shown: high-elevation platform covered by patterned ground (ARP),
899 alluvial fan (CRE) and hummocky moraine and rockfall deposits (SAN). The hillshade area
900 corresponds to bedrock (mainly limestones, as well as shales for the Arpille ridge, see text for
901 details).

902

903 **Figure 3.** Field photographs. **A.** General view of the three study sites (see Fig. 2 for locations)
904 looking from the South (orthophoto and swissALTI3D DEM from swisstopo, authorization
905 5701367467/000010). **B.** High-elevation platform covered by sorted polygonal patterned ground
906 (ARP site), on the southern slope of the Arpelistock peak. Arrows indicate the locations of the
907 two stratigraphic sections and the ARP samples. **C.** View from the Arpille ridge on the Sanetsch
908 valley, with arrows indicating the location of the alluvial-fan log (CRE site) and the hummocky
909 moraine with overlying rockfall deposits (SAN site), in contact with the Sanetsch artificial lake.
910 **D.** Hummocky moraine (SAN site) partially covered by rockfall boulders derived from Les
911 Montons cliff.

912

913 **Figure 4.** Stratigraphy of the ARP site (left: photograph, right: log). Sedimentological units and
914 samples collected for the different analyses are represented: XRD (ARP01 and ARP03, red
915 crossed circles), grain size (G7 and G8, black circles), conventional OSL (ARP01-ARP03, red
916 crossed circles) and portable OSL (arp01-arp05, blue boxes). Unit colours refer to the
917 stratigraphic description in Table S3. The deposit lies on top of non-weathered siliceous-
918 limestone bedrock.

919

920 **Figure 5.** Stratigraphy of the CRE site (left: photograph, right: log). Sedimentological units and
921 samples collected for the different analyses are shown: XRD (CRE01-CRE16, blue boxes), grain
922 size (G1-G6, black circles), micromorphology (M1-M3, black rectangles), conventional OSL
923 (CRE01-CRE04, red crossed circles) and portable OSL (cre01-cre16, blue boxes). Red dashed
924 lines show the extent of the photograph in proportion to the log. Unit colours refer to the
925 stratigraphic description in Table S4.

926

927 **Figure 6.** Grain-size distributions of ARP (G7 and G8, in red) and CRE (G1-G6, in blue)
928 samples. Individual cumulative (top) and frequency (bottom) curves show strong similarities
929 between ARP and CRE sites. The distribution curves of G4 (CRE) and G8 (ARP) are slightly
930 different because of the presence of small clasts within the samples (see individual peak at □ 10^4
931 µm). Grain-size distribution data are reported in Table S6.

932

933 **Figure 7.** Main micromorphological features observed in CRE fine and heterogeneous units (A-
934 C) and bedrock thin section D). **A.** Thin section M1 (unit 6), shows a blocky microstructure

935 developed in the silty sediments expressed by slickensides associated with mottling (reddish
936 zones pointed by yellow arrows). **B.** Detail of thin section M2 showing the well-developed
937 horizontal parallel lamination present within unit 7. **C.** Detail of thin section M3 with weathered,
938 decarbonated lithic fragments containing quartz grains (greyish grains, examples highlighted by
939 yellow arrows), in a clayey-silty carbonated matrix (unit 13). **D.** Bedrock thin section (calcareous
940 shales S1) showing abundant quartz grains (greyish grains, examples highlighted by yellow
941 arrows). xpl = crossed polarized light; ppl = plane polarized light.
942
943 **Figure 8.** XRD bulk mineralogical compositions of CRE (CRE01-CRE16), ARP (ARP01 and
944 ARP03) and bedrock (L1-L2: siliceous limestone, S1-S2: calcareous shale) samples. Cumulative
945 mineral percentages are reported in Table S7.
946
947 **Figure 9.** Portable and conventional luminescence measurements for the ARP site. **A.** OSL
948 signal intensity profile and quartz OSL ages. **B.** IRSL signal intensity profile and polymineral
949 IRSL ages. See Fig. 4 for the legend of the stratigraphic column.
950
951 **Figure 10.** Portable and conventional luminescence measurements for the CRE site. OSL signal
952 intensity profile and quartz OSL ages are shown. See Fig. 5 for the legend of the stratigraphic
953 column.
954
955 **Figure 11.** ^{10}Be surface exposure ages from rock-fall sandstone boulders lying on the hummocky
956 moraine (SAN site, modified orthophoto from swisstopo, authorization 5701367467/000010).
957 ^{10}Be surface exposure ages calculated with snow and erosion corrections are shown. See Table 3

for the ages obtained without applying any correction. The blue dashed-line delimits the extent of a younger rockfall deposit than the one dated in the present study. Inset shows probability density plots of the individual and weighted-average ^{10}Be surface exposure ages, after snow and erosion corrections.

Figure 12. Schematic palaeoenvironmental reconstruction of the study area. **A.** Glacier extent with subglacial sediment deposition, and aeolian drapes deposition on nunatak platforms, during the LGM and Lateglacial periods. **B.** Paraglacial (alluvial, colluvial, lacustrine, aeolian) and periglacial (cryoturbation) geomorphic processes during/soon after glacier retreat, at the Lateglacial-Holocene transition. The three landforms investigated in the study are indicated (ARP, CRE, SAN).

List of Tables

Table 1. Sample luminescence details and corresponding quartz OSL dating results. For analytical details about the measurement protocol, see Table S2A. CAM = Central Age Model; OD = Over Dispersion (Galbraith & Roberts 2012).

Table 2. Sample luminescence details and corresponding polymineral IRSL dating results. See Table 1 (ARP samples) for radionuclides concentration and water content. For analytical details about the measurement protocol, see Table S2B. CAM = Central Age Model; OD = Over Dispersion (Galbraith & Roberts 2012).

980 Table 3. Details on cosmogenic ^{10}Be samples, concentrations and exposure ages. Samples
981 thickness and density are 2.5 cm and 2.65 g cm^{-3}, respectively.

982

983 **Supporting information**

984 Table S1. Samples locations, corresponding geomorphic units and conducted analyses.

985

986 Table S2. Luminescence protocols. A. Post-IR OSL protocol, after Murray & Wintle (2000),
987 applied on quartz separates from CRE and ARP sample (except for sample ARP03, which did
988 not provide enough material for quartz purification). B. Post-IR IRSL protocol, after Buylaert *et*
989 *al.* (2009), applied on polymineral ARP samples. No post-IR IRSL measurements were
990 performed on CRE samples due to the absence of feldspar IRSL signal.

991

992 Table S3. Stratigraphic description and field interpretation of the sedimentological units forming
993 the ARP high-elevation platform deposit. The thickness of the units is given in Fig. 4. *Reaction
994 to HCl on the field: no (-), little (-/+), strong (+), very strong (++) reaction.

995

996 Table S4. Stratigraphic description and field interpretation of the sedimentological units forming
997 the upper 4.5 m of the CRE alluvial fan. The thickness of the units is given in Fig. 5. *Reaction
998 to HCl on the field: no (-), little (-/+), strong (+), very strong (++) reaction.

999

1000 Table S5. Luminescence signal intensities measured for CRE and ARP sites using the SUERC
1001 portable OSL reader (Sanderson & Murphy 2010), and following the measurement sequence of
1002 Muñoz-Salinas *et al.* (2014). IRSL counts are the total photon counts obtained after the first 30 s

of IRSL stimulation. OSL counts are the total photon counts obtained after the 60 s of OSL stimulation. The counts and respective errors were obtained by averaging between two replicate measurements of each bulk sediment sample. Dim IRSL counts were measured along the CRE section, due to the low-feldspar content in the analysed sediments. For this reason, only the OSL signal intensity profile is represented in Fig. 10.

Table S6. Grain-size distributions of CRE (G1-G6; S6A) and ARP (G7 and G8; S6B) samples. Individual cumulative and frequency percentages of the different grain sizes are reported. Details about grain-size distribution measurements are given in the main text.

Table S6A. Grain-size distributions of CRE samples.

Table S6B. Grain-size distributions of ARP samples.

Table S7. XRD bulk mineralogical compositions of CRE (CRE01-CRE16), ARP (ARP01 andARP03) and bedrock (L1-L2: siliceous limestone, S1-S2: calcareous shale) samples. Cumulative mineral percentages are reported. Details about XRD analyses are given in the main text.

1020

List of Figures

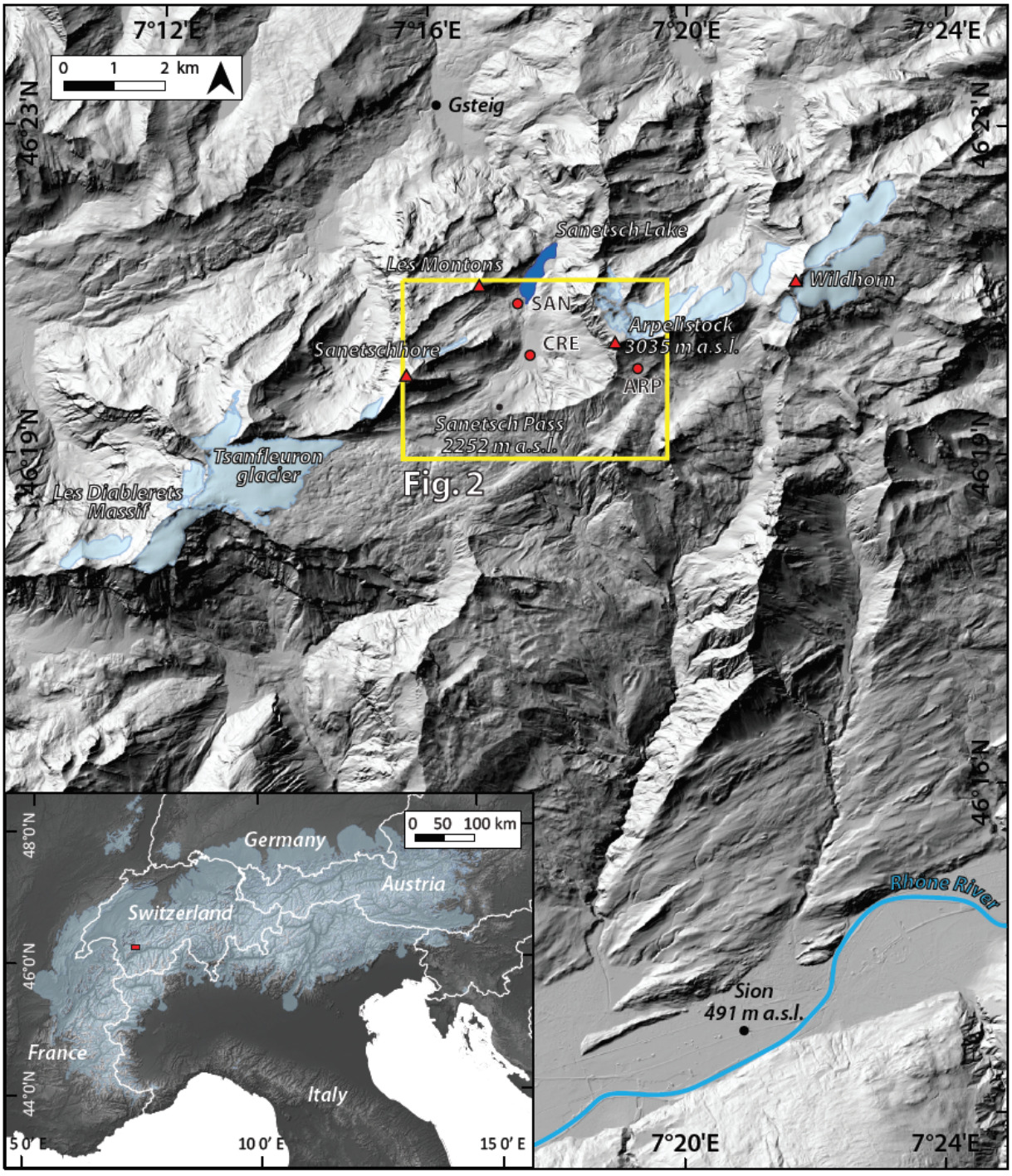

Figure 1. Location of the study area (DEM from swisstopo, authorization 5701367467/000010). Present-day glaciers, main peaks around the Sanetsch Pass and the Rhône River are mapped. The

yellow box indicates the extent of the geomorphological map represented in Figure 2. Inset shows location of the Sanetsch Pass (red box) within Switzerland and the European Alps, with the LGM ice extent (Ehlers and Gibbard, 2004).

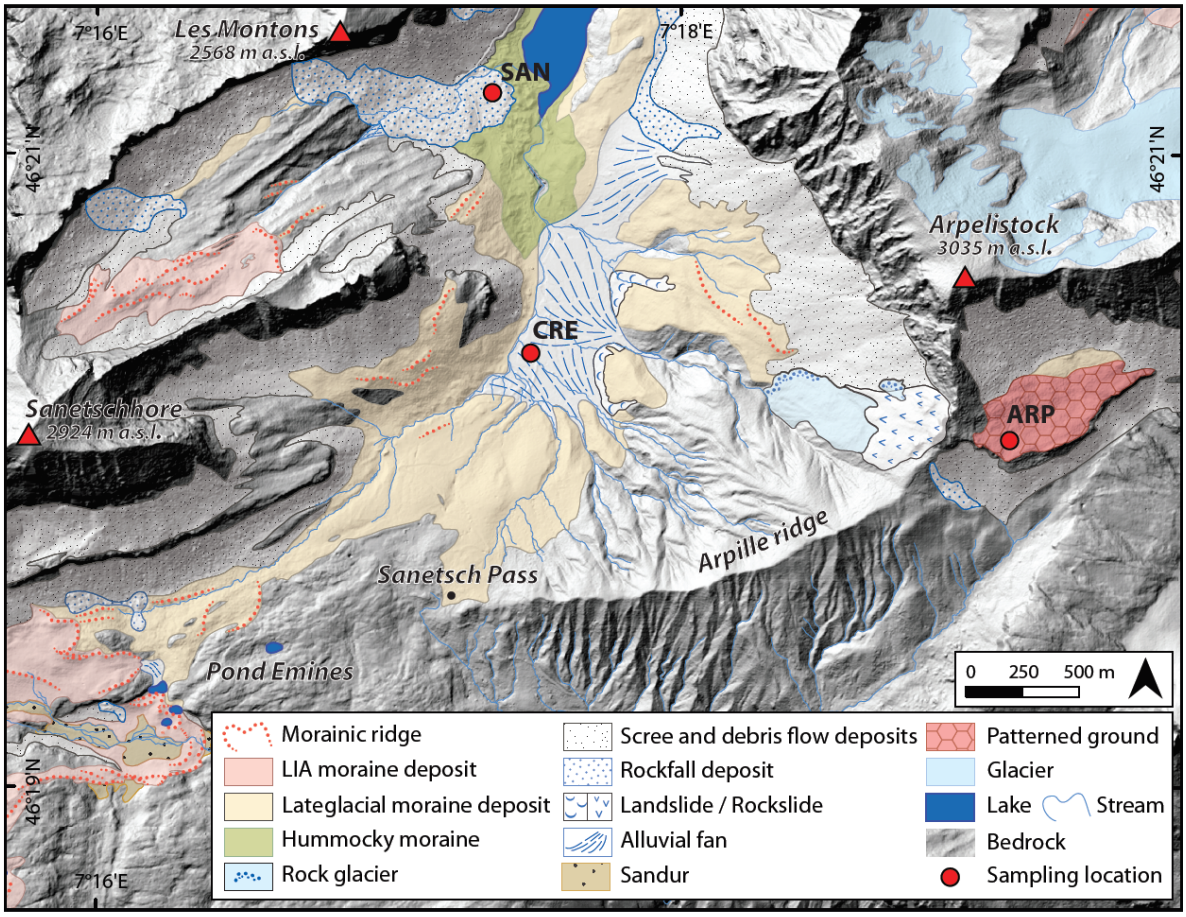

Figure 2. Detailed map of the Quaternary superficial deposits occurring in the study area (swissALTI3D DEM from swisstopo, authorization 5701367467/000010). The different Quaternary deposits and the three study sites are represented: high-elevation platform covered by patterned ground (ARP), alluvial fan (CRE) and hummocky moraine and rockfall deposits (SAN). The hillshade area corresponds to bedrock (mainly limestones, as well as shales for the Arpille ridge, see text for details).

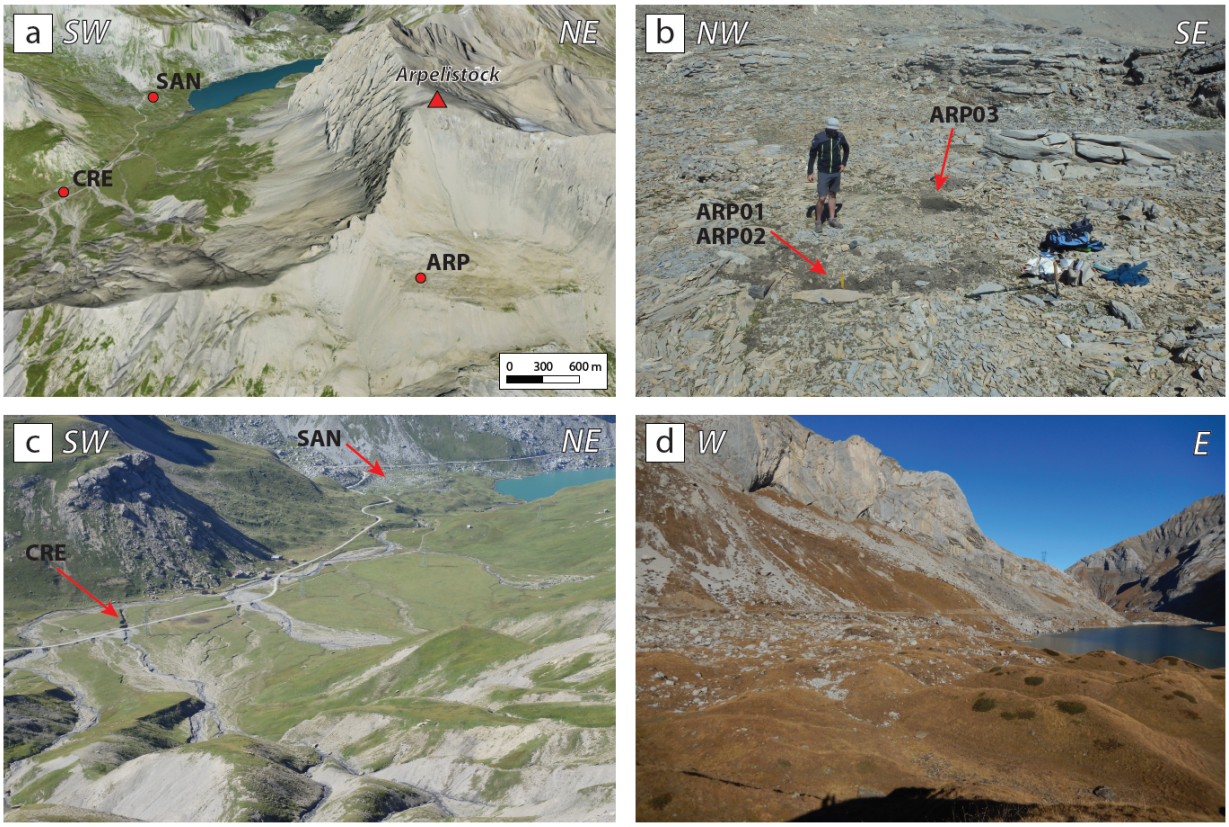

16

17 **Figure 3.** Field photographs. **a)** General view of the three study sites (see Figure 2 for locations)
18 looking from the South (orthophoto and swissALTI3D DEM from swisstopo, authorization
19 5701367467/000010). **b)** High-elevation platform covered by sorted polygonal patterned ground
20 (ARP site), on the southern slope of the Arpelistock peak. Arrows indicate the locations of the
21 two stratigraphic sections and the three ARP samples. **c)** View from the Arpille ridge on the
22 Sanetsch valley, with arrows indicating the location of the alluvial-fan log (CRE site) and the
23 hummocky moraine with overlying rockfall deposits (SAN site), in contact with the Sanetsch
24 artificial lake. **d)** Hummocky moraine (SAN site) partially covered by rockfall boulders derived
25 from Les Montons cliff.

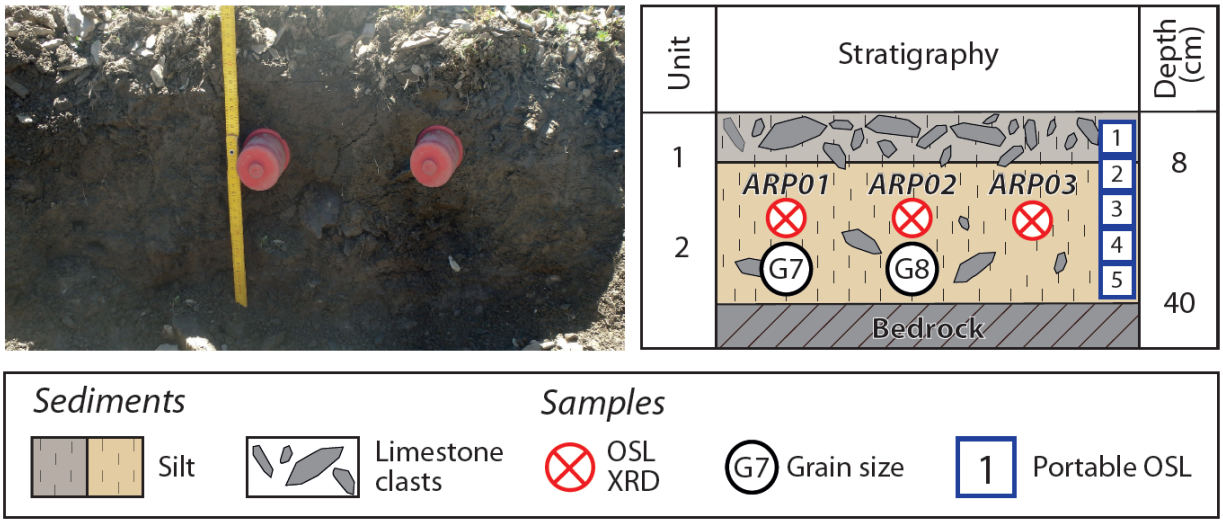

Figure 4. Stratigraphy of the ARP site (left: photograph, right: log). Sedimentological units and samples collected for the different analyses are represented: XRD (ARP01 and ARP03, red crossed circles), grain size (G7 and G8, black circles), conventional OSL (ARP01-ARP03, red crossed circles) and portable OSL (arp01-arp05, blue boxes). Unit colours refer to the stratigraphic description in Table S3. The deposit lies on top of non-weathered siliceous-limestone bedrock.

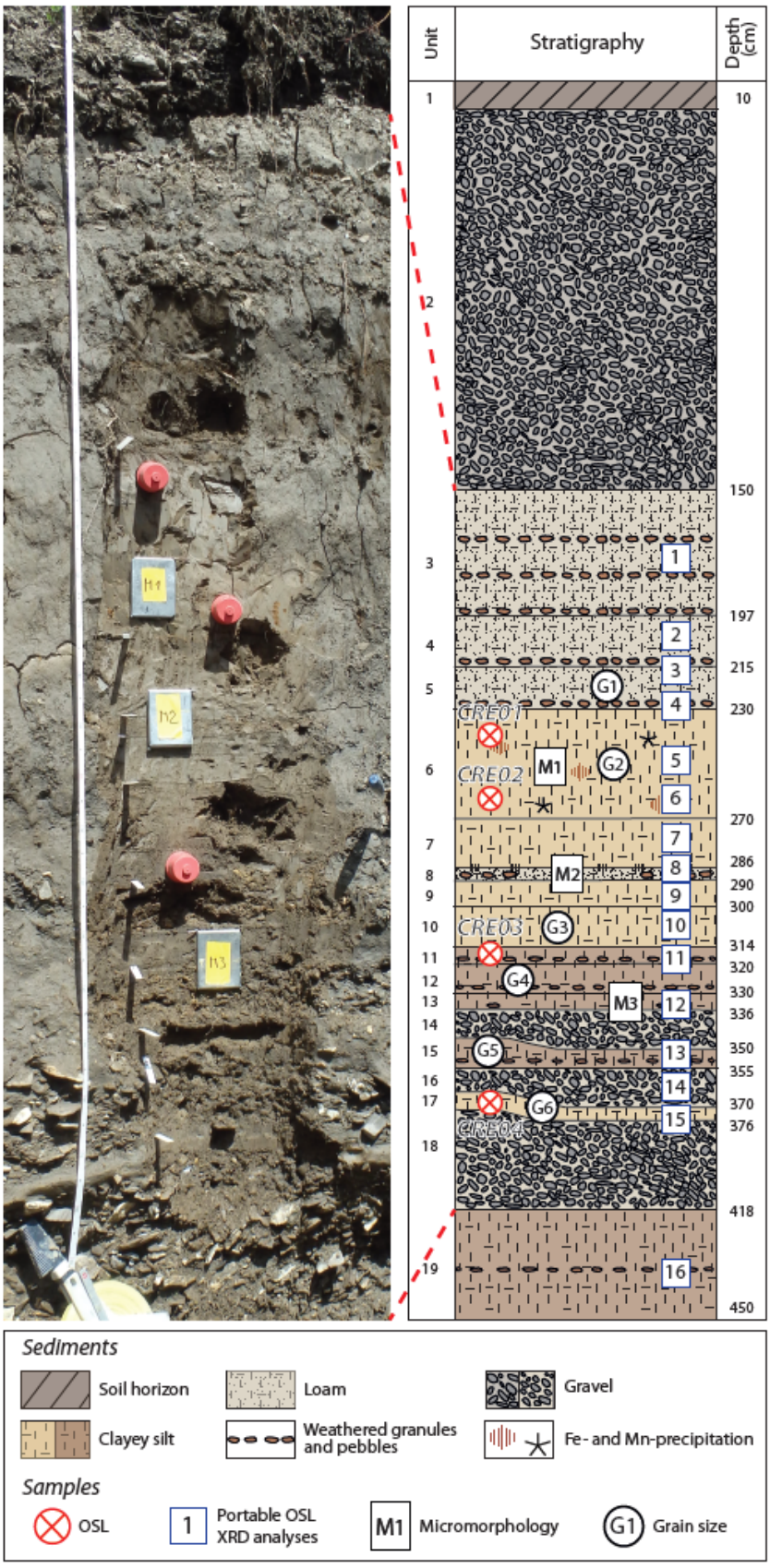
Unit
Stratigraphy
Depth (cm)
1
2
3
4
5
6
7
8
9
10
11
12
13
14
15
16
17
18
19
10
150
197
215
230
270
286
290
300
314
320
330
336
350
355
370
376
418
450
CRE01
CRE02
CRE03
CRE04
M1
M2
M3
G1
G2
G3
G4
G5
G6
Sediments
Soil horizon
Loam
Gravel
Clayey silt
Weathered granules and pebbles
Fe- and Mn-precipitation
Samples
OSL
Portable OSL
XRD analyses
Micromorphology
Grain size

Figure 5. Stratigraphy of the CRE site (left: photograph, right: log). Sedimentological units and samples collected for the different analyses are shown: XRD (CRE01-CRE16, blue boxes), grain size (G1-G6, black circles), micromorphology (M1-M3, black rectangles), conventional OSL (CRE01-CRE04, red crossed circles) and portable OSL (cre01-cre16, blue boxes). Red dashed lines show the extent of the picture in proportion to the log. Unit colours refer to the stratigraphic description in Table S4.

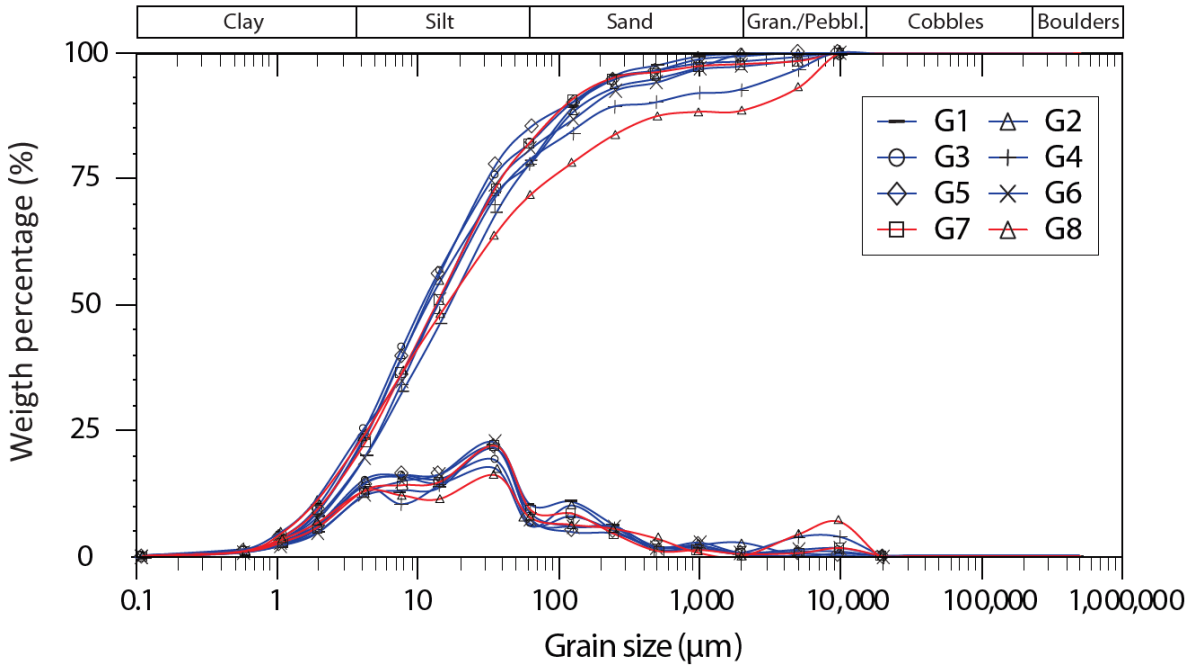

Figure 6. Grain-size distributions of ARP (G7 and G8, in red) and CRE (G1-G6, in blue) samples. Individual cumulative (top) and frequency (bottom) curves are plotted, and show strong similarities between ARP and CRE sites. The distribution curves of G4 (CRE) and G8 (ARP) are slightly different because of the presence of small clasts within the samples (see individual peak at ca. 10^4 µm).

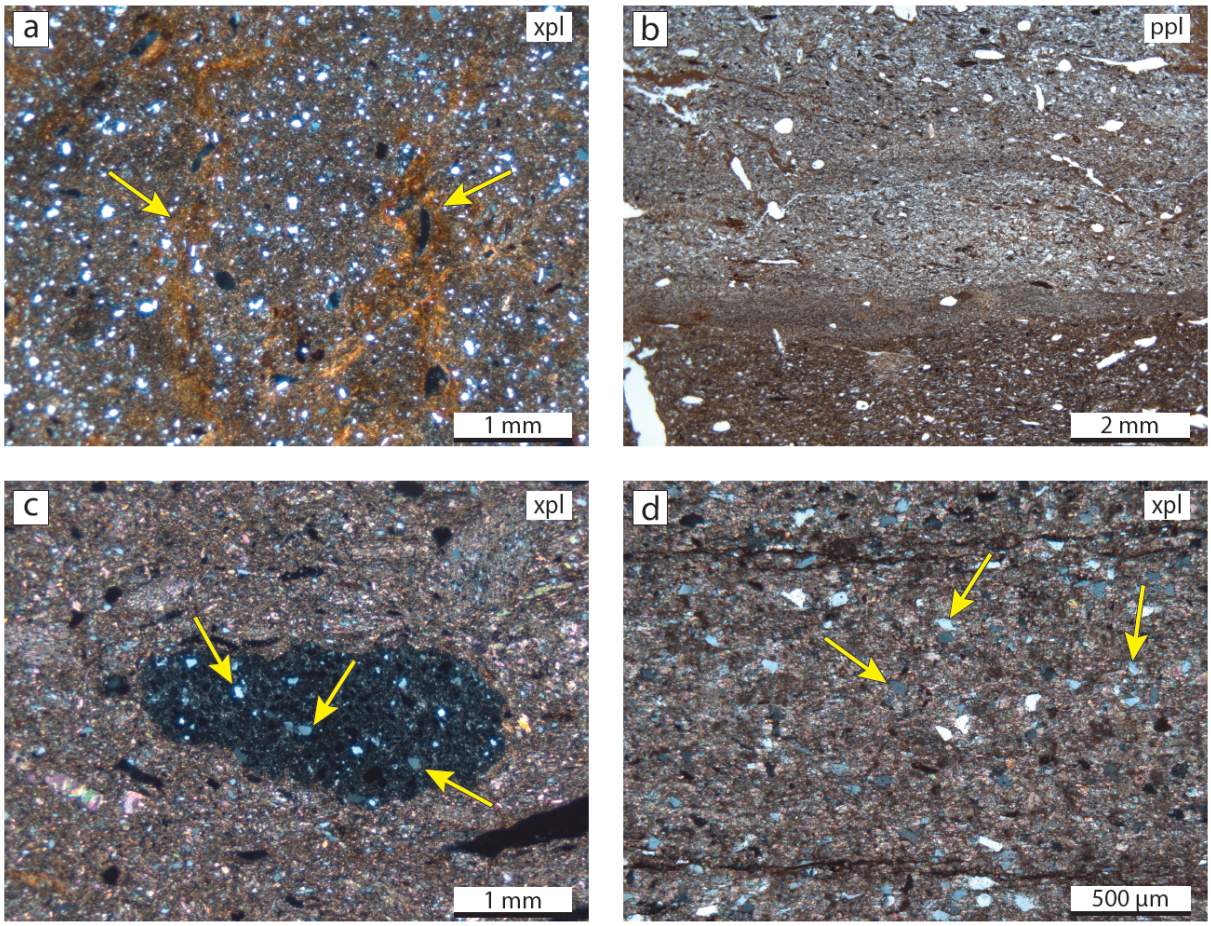

Figure 7. Main micromorphological features observed in CRE fine and heterogeneous units (a-c) and bedrock thin section (d). **a)** Thin section M1 (unit 6), shows a blocky microstructure developed in the silty sediments expressed by slickensides associated with mottling (reddish zones pointed by yellow arrows). **b)** Detail of thin section M2 showing the well-developed horizontal parallel lamination present within unit 7. **c)** Detail of thin section M3 with weathered, decarbonated lithic fragments containing quartz grains (greyish grains, examples highlighted by yellow arrows), in a clayey-silty carbonated matrix (unit 13). **d)** Bedrock thin section (calcareous shales S1) showing abundant quartz grains (greyish grains, examples highlighted by yellow arrows). xpl: crossed polarized light; ppl: plane polarized light.

Figure 8. XRD bulk mineralogical compositions of CRE (CRE01-CRE16), ARP (ARP01 and ARP03) and bedrock (L1-L2: siliceous limestone, S1-S2: calcareous shale) samples.

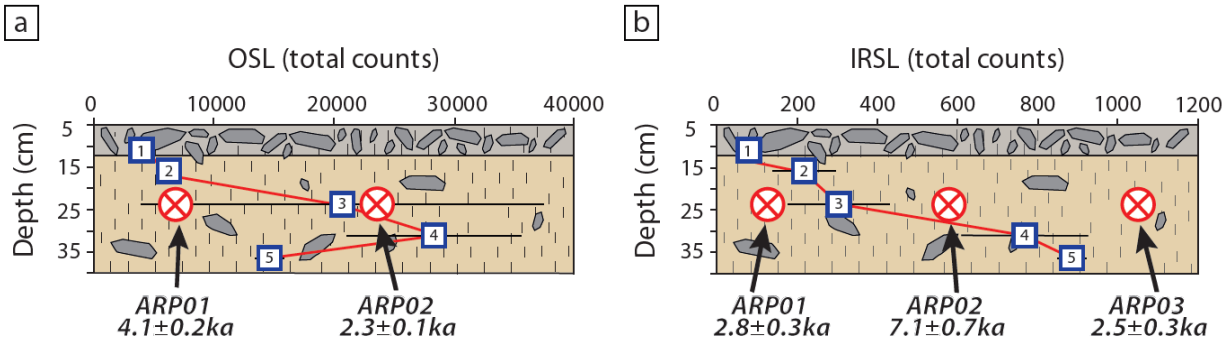

Figure 9. Portable and conventional luminescence measurements for the ARP site. **a)** OSL signal intensity profile and quartz OSL ages. **b)** IRSL signal intensity profile and polymineral IRSL ages. The reader is referred to Figure 4 for the legend of the stratigraphic column.

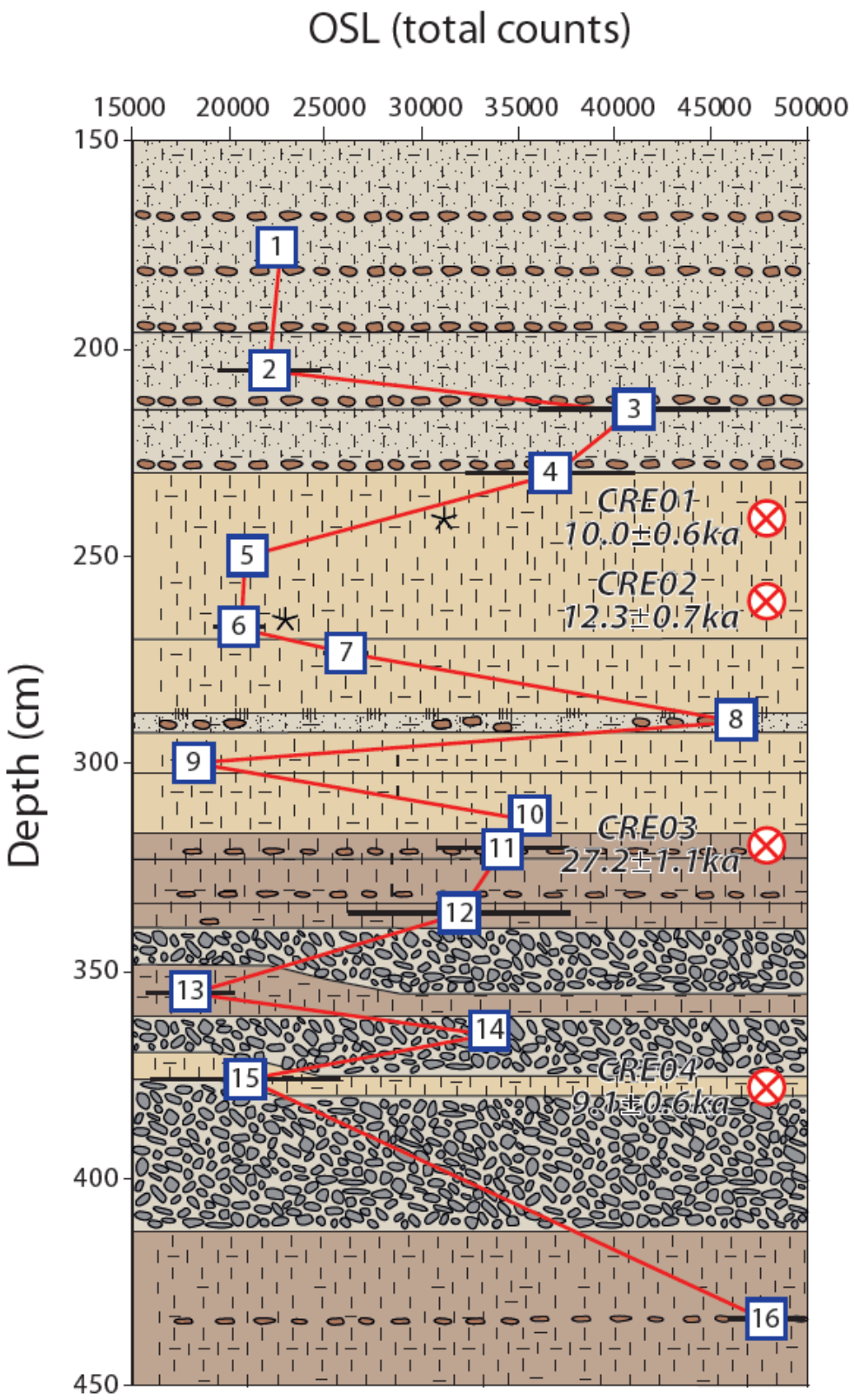
OSL (total counts)
15000
20000
25000
30000
35000
40000
45000
50000
Depth (cm)
150
200
250
300
350
400
450
1
2
3
4
5
6
7
8
9
10
11
12
13
14
15
16
CRE01
10.0±0.6ka
CRE02
12.3±0.7ka
CRE03
27.2±1.1ka
CRE04
9.1±0.6ka

Figure 10. Portable and conventional luminescence measurements for the CRE site. OSL signal intensity profile and quartz OSL ages are shown. The reader is referred to Figure 5 for the legend of the stratigraphic column.

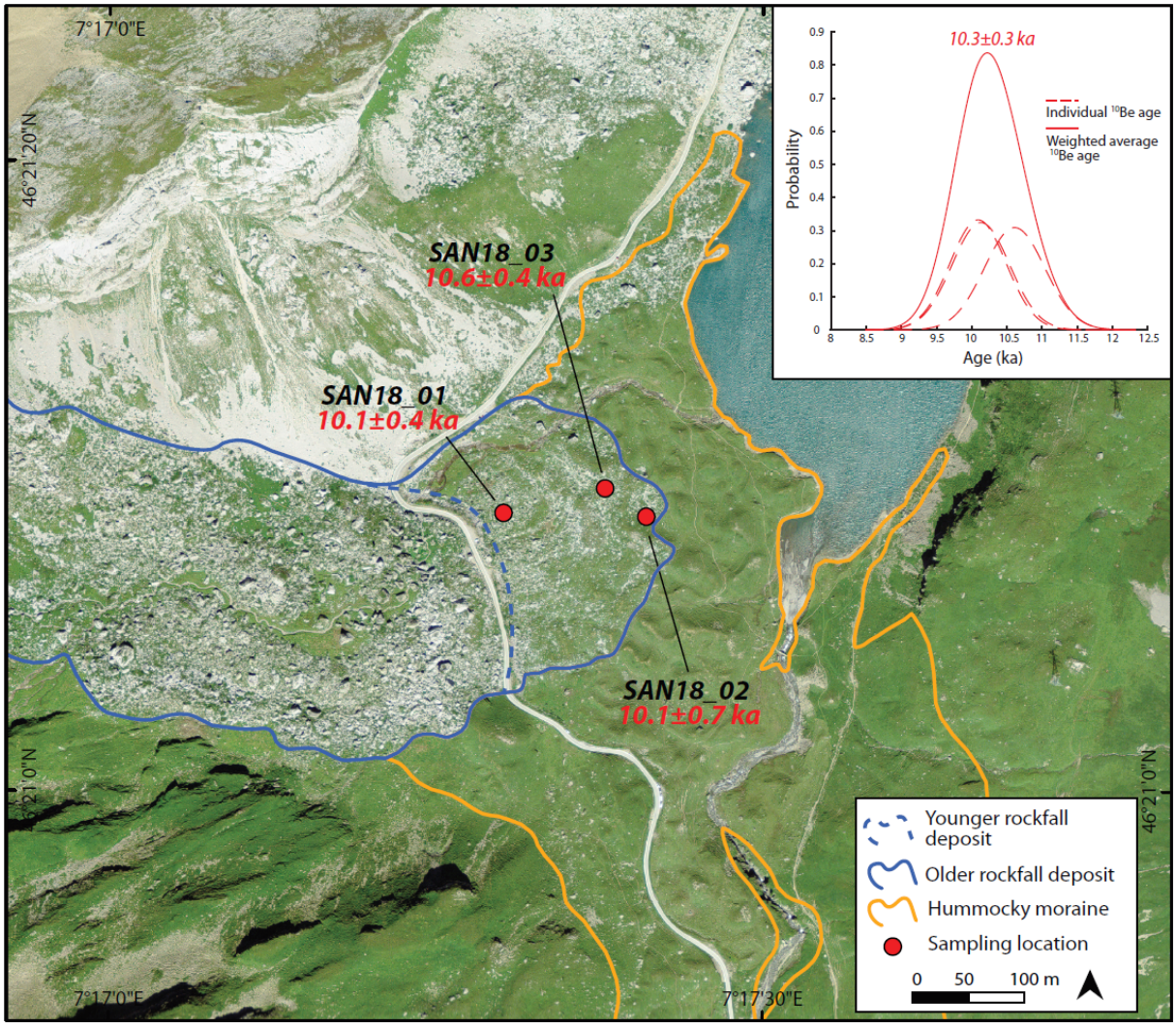

Figure 11. ^{10}Be surface exposure ages from rock-fall sandstone boulders lying on the hummocky moraine (SAN site, modified orthophoto from swisstopo, authorization 5701367467/000010). ^{10}Be surface exposure ages calculated with snow and erosion corrections are shown. The reader is referred to Table 3 for the ages obtained without applying any correction. The blue dashed-line

delimits the extent of a younger rockfall deposit than the one dated in the present study. Inset shows probability density plots of the individual and weighted-average ^{10}Be surface exposure ages, after snow and erosion corrections.

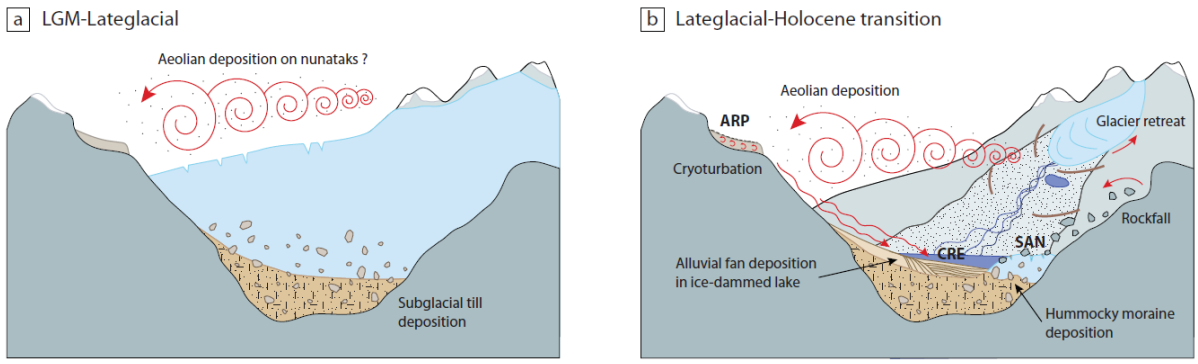

Figure 12. Schematic paleo-environmental reconstruction of the study area. **a)** Glacier extent with sub-glacial sediment deposition, and aeolian drapes deposition on nunatak platforms, during the LGM and Lateglacial periods. **b)** Paraglacial (alluvial, colluvial, lacustrine, aeolian) and periglacial (cryoturbation) geomorphic processes during/soon after glacier retreat, at the Lateglacial-Holocene transition. The three landforms investigated in the study are indicated (ARP, CRE, SAN).

92 **List of Tables**

93 **Table 1.** Sample luminescence details and corresponding quartz OSL dating results. For analytical details about the measurement

94 protocol, see Supplementary Table S2a.

95 *CAM: Central Age Model, **OD: Over Dispersion (Galbraith & Roberts 2012).

Sample	Depth below surface (m)	Radionuclide concentration			Water content (%)	Total dose rate (Gy ka^{-1})	CAM* D_e (Gy)	Aliquots number	OD** (%)	Age (ka)
		U (ppm)	Th (ppm)	K (%)						
ARP01	0.15	3.4±0.2	10.5±0.5	1.6±0.1	18	3.53±0.13	14.51±0.45	11	8.6	4.1±0.2
ARP02	0.15	3.4±0.2	10.5±0.5	1.6±0.1	18	3.53±0.13	8.14±0.36	12	14.7	2.3±0.1
CRE01	2.35	3.2±0.2	12.0±0.6	1.8±0.1	28	3.36±0.12	33.45±1.51	12	15.1	10.0±0.6
CRE02	2.65	3.4±0.3	11.7±0.6	1.8±0.1	27	3.40±0.13	41.90±1.78	12	14.0	12.3±0.7
CRE03	3.17	2.9±0.2	10.4±0.5	1.6±0.1	33	2.89±0.10	78.44±1.71	12	4.5	27.2±1.1
CRE04	3.73	3.1±0.2	10.3±0.5	1.8±0.1	31	3.08±0.11	28.18±1.38	7	8.9	9.1±0.6

96

97

98

99

100

101

Table 2. Sample luminescence details and corresponding polymineral IRSL dating results. The reader is referred to Table 1 (ARP samples) for radionuclides concentration. For analytical details about the measurement protocol, see Supplementary Table S2b.

*CAM: Central Age Model, **OD: Over Dispersion (Galbraith & Roberts 2012).

Sample	Depth below surface (m)	Total dose rate (Gy ka^{-1})	CAM* Uncorrected D_e (Gy)	Aliquots number	OD** (%)	g_{2days} (%/decade)	CAM* Corrected D_e (Gy)	Age (ka)
ARP01	0.15	4.13±0.15	10.57±0.35	11	0	1.26±1.03	11.77±1.21	2.8±0.3
ARP02	0.15	4.13±0.15	26.01±1.02	10	9.82	1.39±0.88	29.50±2.88	7.1±0.7
ARP03	0.15	4.13±0.15	9.02±0.47	12	14.47	1.43±0.98	10.19±1.08	2.5±0.3

115 **Table 3.** Details on cosmogenic ^{10}Be samples, concentrations and exposure ages. Samples thickness and density are 2.5 cm and 2.65 g
116 cm^{-3}, respectively.
117 *Topographic shielding correction according to Dunne *et al.* (1999).
118 **^{10}Be production rate of 4.16±0.10 at.g^{-1} yr^{-1} (Claude *et al.* 2014) and LSDn scaling scheme (Lifton *et al.* 2014).
119 ***50 cm snow cover for 6 months per year (Wirsig *et al.* 2016a), snow density of 0.3 g cm^{-3} and spallation attenuation length in
120 snow of 109 g cm^{-2} (Delunel *et al.* 2014). Erosion rate of 1 mm ka^{-1} (Wirsig *et al.* 2016b; Wirsig *et al.* 2016a).

Sample	Location WGS 84 (°N/°E)	Elevation (m a.s.l.)	Topographic shielding*	^{10}Be/^{9}Be blank corrected (10^{-13} at g^{-1})	^{10}Be/^{9}Be uncertainty (%)	^{10}Be concentration (10^{5} at g^{-1})	^{10}Be exposure age (ka)**	
							no snow/erosion	incl. snow/erosion***
SAN18_01	46.35111/ 7.28751	2055	0.92	1.46	3.33	1.86±0.06	9.3±0.4	10.1±0.4
SAN18_02	46.35117/ 7.28900	2056	0.96	1.55	3.38	1.96±0.07	9.4±0.4	10.1±0.4
SAN18_03	46.35137/ 7.28874	2054	0.94	1.76	3.39	2.01±0.07	9.8±0.4	10.6±0.4

121

Table S1. Samples locations, corresponding geomorphic units and conducted analyses.

Sample Name	Location WGS84 (°N/°E)	Altitude (m a.s.l.)	Geomorphic unit	Analysis
G1 - G6	46.34091/ 7.29049	2100	Alluvial fan (CRE)	Grain-size
G7, G8	46.33703/ 7.31810	2712	High-elevation platform (ARP)	Grain-size
M1 - M3	46.34091/ 7.29049	2100	Alluvial fan (CRE)	Micromorphology
L1, L2; S1, S2	46.33715/ 7.31815; 46.33380/ 7.30790	2712; 2650	Bedrock (limestone; shale)	Petrographic thin section
CRE01 - CRE16	46.34091/ 7.29049	2100	Alluvial fan (CRE)	XRD and Geochemistry
ARP01, ARP03	46.33703/ 7.31810	2712	High-elevation platform (ARP)	XRD and Geochemistry
L1, L2; S1, S2	46.33715/ 7.31815; 46.33380/ 7.30790	2712; 2650	Bedrock (limestone; shale)	XRD
cre01 - cre16	46.34091/ 7.29049	2100	Alluvial fan (CRE)	Portable OSL
arp01 - arp05	46.33703/ 7.31810	2712	High-elevation platform (ARP)	Portable OSL
CRE01 - CRE04	46.34091/ 7.29049	2100	Alluvial fan (CRE)	OSL burial dating
ARP01 - ARP03	46.33703/ 7.31810	2712	High-elevation platform (ARP)	OSL burial dating
SAN01	46.35111/ 7.28751	2055	Rockfall deposit (SAN)	^{10}Be exposure dating
SAN02	46.35117/ 7.28900	2056	Rockfall deposit (SAN)	^{10}Be exposure dating
SAN03	46.35137/ 7.28874	2054	Rockfall deposit (SAN)	^{10}Be exposure dating

Table S2. Luminescence protocols. **A.** Post-IR OSL protocol, after Murray & Wintle (2000), applied on quartz separates from CRE and ARP sample (except for sample ARP03, which did not provide enough material for quartz purification). **B.** Post-IR IRSL protocol, after Buylaert *et al.* (2009), applied on polymineral ARP samples. No post-IR IRSL measurements were performed on CRE samples due to the absence of feldspar IRSL signal.

Table S2A

Step	Treatment	
1	Natural/regenerative dose	
2	Preheat	200°C, 60 s
3	IRSL	50°C, 100 s
4	OSL	125°C, 100 s
5	Test dose	500 s
6	Preheat	200°C, 60 s
7	IRSL	50°C, 100 s
8	OSL	125°C, 100 s
9	Return to step 1	

Table S2B

Step	Treatment	
1	Natural/regenerative dose	
2	Preheat	250°C, 60 s
3	IRSL	50°C, 100 s
4	IRSL	225°C, 100 s
5	Test dose	500 s
6	Preheat	250°C, 60 s
7	IRSL	50°C, 100 s
8	IRSL	225°C, 100 s
9	IRSL	290°C, 40 s
10	Return to step 1	

16 **Table S3.** Stratigraphic description and field interpretation of the sedimentological units forming the ARP high-elevation platform
17 deposit. The thickness of the units is given in Fig. 4. *Reaction to HCl on the field: no (-), little (-/+), strong (+), very strong (++)
18 reaction.

Unit	Description	HCl*	Field interpretation
1	Angular platy fragments of grey siliceous limestones (60%) in a greyish brown silty matrix (40%). Clast-supported, no preferred orientation of elements. Well-developed forms of sorted polygonal patterned grounds on the surface.	-	*In situ* cryoclasts bedrock derived, reworked by frost and thaw processes.
2	Light yellowish brown silt containing few limestone angular fragments. Well-developed platy structure.	++	Aeolian deposit.

19

Table S4. Stratigraphic description and field interpretation of the sedimentological units forming the upper 4.5 m of the CRE alluvial fan. The thickness of the units is given in Fig. 5. *Reaction to HCl on the field: no (-), little (-/+), strong (+), very strong (++) reaction.

Unit	Description	HCl*	Field interpretation
1	Dark brown humic loam containing platy fragments of shale. Granular structure.	-	Current A horizon of a soil developed under an alpine meadow.
2	Platy subangular fragments (mean diameter 5-10 cm, max. 30 cm) of slightly weathered shale (ca. 70%) in a greyish brown loamy matrix (ca. 30%). Clast-supported with imbricated elements.	++	Coarse alluvial fan deposit.
3	Three sub-units each composed of slightly weathered granules and pebbles (shale and limestone) at the base and yellowish to grayish brown silty loam at the top.	++	Alluvial fining-up sedimentary sequences possibly deposited in a lake.
4, 5	Orange strongly weathered (almost decarbonated) pebbles (shale and limestone) at the base, light yellowish to grayish brown silty loam at the top.	-/+	Alluvial fining-up sedimentary sequences possibly deposited in a lake (affected by pre- or post-depositional weathering).
6	Light yellowish brown clayey silt with black and red mottles (Fe-Mn hydromorphism) especially at the base. Massive structure.	-	Aeolian sediments (in situ deposited or reworked by fluvial transport).
7, 9, 10, 17	Yellowish to grayish brown clayey silt. Massive structure, less consistent than unit 6. Laterally, presence of isolated pebbles and cobbles in units 7, 9 and 10.	-	Aeolian sediments possibly deposited or reworked in a lake, with possible dropstones (10-15 cm).
8	Yellowish brown sandy loam containing orange weathered calcareous granules.	-/+	Alluvial input (affected by pre- or post-depositional weathering).

11, 12, 13	Greyish brown silty clay with strongly weathered (decarbonated) granules and pebbles at the base. Massive structure, very low consistency.	-/+	
15, 19	Similar to above but with little weathering of the pebbles.	++	Alluvial input.
14, 16, 18	Grey calcareous pebbles and granules (ca 60%) in a yellowish brown loamy matrix (40%). Clast-supported sediment with weathered imbricated elements.	++	

Table S5. Luminescence signal intensities measured for CRE and ARP sites using the SUERC portable OSL reader (Sanderson & Murphy 2010), and following the measurement sequence of Muñoz-Salinas *et al.* (2014). IRSL counts are the total photon counts obtained after the first 30 s of IRSL stimulation. OSL counts are the total photon counts obtained after the 60 s of OSL stimulation. The counts and respective errors were obtained by averaging between two replicate measurements of each bulk sediment sample. Dim IRSL counts were measured along the CRE section, due to the low-feldspar content in the analysed sediments. For this reason, only the OSL signal intensity profile is represented in Fig. 10.

Sample	Depth (cm)	IRSL (counts)	OSL (counts)
cre01	175	79±24	22697±154
cre02	205	68±24	22062±2674
cre03	215	268±76	40924±4946
cre04	230	218±42	36925±4341
cre05	250	250±45	20808±931
cre06	267	227±89	20620±1260
cre07	273	196±51	26092±1162
cre08	290	142±42	46407±667
cre09	300	187±26	18210±497
cre10	314	203±116	35955±1162
cre11	320	96±116	34252±3459
cre12	336	264±122	31968±5749
cre13	355	210±83	18034±2269
cre14	365	256±48	33525±806
cre15	376	58±74	20950±4965
cre16	420	210±79	47951±1995
arp01	10	75±21	3668±407
arp02	17	213±94	5965±351
arp03	24	303±152	20339±16682
arp04	31	768±190	28319±7321
arp05	38	883±43	14250±1201

Table S6. Grain-size distributions of CRE (G1-G6; S6A) and ARP (G7 and G8; S6B) samples. Individual cumulative and frequency percentages of the different grain sizes are reported. Details about grain-size distribution measurements are given in the main text.

Table S6A. Grain-size distributions of CRE samples.

Sample	G1		G2		G3		G4		G5		G6	
Grain size (μm)	Cumulative (%)	Frequency (%)	Cumulative (%)	Frequency (%)	Cumulative (%)	Frequency (%)	Cumulative (%)	Frequency (%)	Cumulative (%)	Frequency (%)	Cumulative (%)	Frequency (%)
0.11	0.00	0.00	0.00	0.00	0.00	0.00	0.00	0.00	0.00	0.00	0.00	0.00
0.58	0.91	0.91	0.95	0.95	1.04	1.04	1.30	1.30	0.96	0.96	0.85	0.85
1.06	3.09	2.18	3.36	2.40	3.74	2.70	4.16	2.86	3.29	2.33	2.80	1.95
1.95	7.99	4.90	9.07	5.72	10.02	6.28	10.24	6.08	8.89	5.60	7.38	4.57
4.19	19.93	11.94	23.76	14.69	25.21	15.19	23.87	13.63	23.35	14.46	19.66	12.28
7.72	32.97	13.04	39.65	15.89	41.29	16.07	34.12	10.25	39.51	16.16	34.56	14.90
14.22	46.51	13.53	54.23	14.58	56.60	15.31	48.11	14.00	55.80	16.29	50.87	16.30
35.56	68.44	21.94	71.81	17.58	75.66	19.06	69.41	21.30	77.41	21.61	73.50	22.63
63	78.70	10.26	77.80	5.99	82.10	6.44	77.90	8.49	85.00	7.59	80.80	7.30
125	89.50	10.80	87.90	10.10	90.00	7.90	83.70	5.80	89.90	4.90	86.60	5.80
250	95.70	6.20	92.90	5.00	95.00	5.00	89.10	5.40	94.50	4.60	92.40	5.80
500	97.70	2.00	94.70	1.80	96.40	1.40	90.10	1.00	96.30	1.80	94.10	1.70
1000	99.50	1.80	96.90	2.20	97.80	1.40	92.00	1.90	98.50	2.20	96.70	2.60

2000	99.90	0.40	99.50	2.60	98.20	0.40	92.60	0.60	99.10	0.60	97.30	0.60
5000	100.00	0.10	99.60	0.10	99.10	0.90	96.30	3.70	99.80	0.70	98.50	1.20
10000	100.00	0.00	100.00	0.40	100.00	0.90	100.00	3.70	100.00	0.20	100.00	1.50
20000	100.00	0.00	100.00	0.00	100.00	0.00	100.00	0.00	100.00	0.00	100.00	0.00
30000	100.00	0.00	100.00	0.00	100.00	0.00	100.00	0.00	100.00	0.00	100.00	0.00
40000	100.00	0.00	100.00	0.00	100.00	0.00	100.00	0.00	100.00	0.00	100.00	0.00
50000	100.00	0.00	100.00	0.00	100.00	0.00	100.00	0.00	100.00	0.00	100.00	0.00
60000	100.00	0.00	100.00	0.00	100.00	0.00	100.00	0.00	100.00	0.00	100.00	0.00
80000	100.00	0.00	100.00	0.00	100.00	0.00	100.00	0.00	100.00	0.00	100.00	0.00
100000	100.00	0.00	100.00	0.00	100.00	0.00	100.00	0.00	100.00	0.00	100.00	0.00
200000	100.00	0.00	100.00	0.00	100.00	0.00	100.00	0.00	100.00	0.00	100.00	0.00
300000	100.00	0.00	100.00	0.00	100.00	0.00	100.00	0.00	100.00	0.00	100.00	0.00
400000	100.00	0.00	100.00	0.00	100.00	0.00	100.00	0.00	100.00	0.00	100.00	0.00
500000	100.00	0.00	100.00	0.00	100.00	0.00	100.00	0.00	100.00	0.00	100.00	0.00

Table S6B. Grain-size distributions of ARP samples.

Sample	G7		G8	
Grain size (μm)	Cumulative (%)	Frequency (%)	Cumulative (%)	Frequency (%)
0.11	0.00	0.00	0.00	0.00
0.58	0.91	0.91	1.11	1.11
1.06	3.62	2.72	4.53	3.42
1.95	9.50	5.88	11.39	6.86
4.19	22.65	13.15	24.35	12.96
7.72	36.76	14.11	36.46	12.11
14.22	51.55	14.79	47.88	11.42
35.56	73.43	21.88	63.97	16.09
63	82.50	9.07	71.80	7.83
125	90.90	8.40	78.20	6.40
250	95.20	4.30	83.80	5.60
500	96.20	1.00	87.50	3.70
1000	97.40	1.20	88.40	0.90
2000	97.80	0.40	88.60	0.20
5000	98.40	0.60	93.00	4.40
10000	100.00	1.60	100.00	7.00
20000	100.00	0.00	100.00	0.00
30000	100.00	0.00	100.00	0.00
40000	100.00	0.00	100.00	0.00
50000	100.00	0.00	100.00	0.00
60000	100.00	0.00	100.00	0.00
80000	100.00	0.00	100.00	0.00
100000	100.00	0.00	100.00	0.00
200000	100.00	0.00	100.00	0.00
300000	100.00	0.00	100.00	0.00

400000	100.00	0.00	100.00	0.00
500000	100.00	0.00	100.00	0.00

Table S7. XRD bulk mineralogical compositions of CRE (CRE01-CRE16), ARP (ARP01 andARP03) and bedrock (L1-L2: siliceous limestone, S1-S2: calcareous shale) samples. Cumulative mineral percentages are reported. Details about XRD analyses are given in the main text.

Sample	Quartz (%)	Micas (%)	Chlorite (%)	Albite (%)	Calcite (%)	Dolomite (%)
CRE01	36.9	42.5	10.6	0.0	10.0	0.0
CRE02	39.2	51.5	9.3	0.0	0.0	0.0
CRE03	50.0	36.0	14.0	0.0	0.0	0.0
CRE04	42.7	22.5	9.9	11.1	13.9	0.0
CRE05	54.4	41.8	3.8	0.0	0.0	0.0
CRE06	46.5	41.3	12.2	0.0	0.0	0.0
CRE07	46.7	40.5	12.8	0.0	0.0	0.0
CRE08	51.4	40.6	8.0	0.0	0.0	0.0
CRE09	41.1	50.8	8.1	0.0	0.0	0.0
CRE10	52.9	39.5	7.6	0.0	0.0	0.0
CRE11	54.0	44.9	1.1	0.0	0.0	0.0
CRE12	43.3	36.1	8.4	0.0	12.3	0.0
CRE13	41.6	38.2	7.9	0.0	12.3	0.0
CRE14	32.4	22.9	6.3	0.0	38.5	0.0
CRE15	41.8	42.9	9.8	0.0	5.5	0.0
CRE16	35.6	30.3	7.4	0.0	26.6	0.0

ARP01	69.6	18.9	7.6	3.9	0.0	0.0
ARP03	66.7	18.2	8.0	7.1	0.0	0.0
L1	25.6	5.6	0.0	0.0	63.7	5.2
L2	32.7	3.0	0.0	0.0	64.3	0.0
S1	23.7	15.5	0.8	0.0	55.1	4.9
S2	22.5	7.0	4.0	0.0	65.9	0.9